A multispectroscopic approach for ultra-trace sensing of prostate specific antigen (PSA) by iron nanocomposite fabricated on graphene nanoplatelet

Shalmali Basu [a], Debashree Das [a], Zarina Ansari [a], Nabakumar Rana [b], Bhim Majhi [c],
Dipendu Patra [c], Ajay Kanungo [c], David Morgan [d], Sanjay Dutta [c], Kamalika Sen [a,*]

[a] *Department of Chemistry, University of Calcutta, 92, APC Road, Kolkata 700009, India*
[b] *Department of Physics, University of Calcutta, 92, APC Road, Kolkata 700009, India*
[c] *Department of Organic and Medicinal Chemistry, CSIR-Indian Institute of Chemical Biology, 4, Raja S. C. Mullick Road, Kolkata 700032, WB, India*
[d] *Cardiff Catalysis Institute, School of Chemistry, Cardiff University, Park Place, Cardiff CF10 3AT, UK*

HIGHLIGHTS

- Graphene modified quinoxaline derivative based iron nanocomposite (1d-Fe-Gr) have been synthesized.
- Spectroscopic sensing of cancer biomarker, PSA in serum medium is done.
- LOD was detected using UV–vis and Raman spectroscopic methods.
- In presence of glucose, cholesterol, bilirubin and insulin, LOD is even lowered.
- PSA and the 1d-Fe-Gr interactions were established using fluorescence, Raman and CD spectroscopy.

GRAPHICAL ABSTRACT

ARTICLE INFO
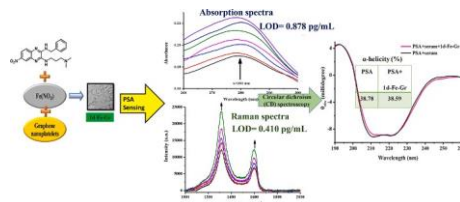
ABSTRACT

Herein we report an easy, rapid and cost-effective method for spectroscopic sensing of a prostate cancer biomarker prostate specific antigen (PSA) using a novel nanocomposite. The material is a synthetic quinoxaline derivative-based iron nanocomposite fabricated on graphene nanoplatelet surface (1d-Fe-Gr). Presence of gra- phene enhanced the efficacy of synthesized 1d-Fe-Gr to sense PSA in serum medium with an impressive limit of detection (LOD) value of 0.878 pg/mL compared to 1d-Fe alone (LOD 17.619 pg/mL) using UV–visible absorption spectroscopy. LOD of PSA by 1d-Fe-Gr using Raman spectroscopy is even more impressive (0.410 pg/mL). Moreover, presence of interfering biomolecules like glucose, cholesterol, bilirubin and insulin in serum improves the detection threshold significantly in presence of 1d-Fe-Gr which otherwise cause LOD values of PSA to elevate in control sets. In presence of these biomolecules, the LOD values improve significantly as compared to healthy conditions in the range 0.623–3.499 pg/mL. Thus, this proposed detection method could also be applied efficiently to the patients suffering from different pathophysiological disorders. These biomolecules may also be added externally during analyses to improve the sensing ability. Fluorescence, Raman and circular dichroism spectroscopy were used to study the underlying mechanism of PSA sensing by 1d-Fe-Gr. Molecular docking studies confirm the selective interaction of 1d-Fe-Gr with PSA over other cancer biomarkers.

* Corresponding author.
E-mail address: kschem@caluniv.ac.in (K. Sen).

1. Introduction

Quinoxaline, also known as benzopyrazine for the presence a ring complex comprising of two aromatic rings named benzene and pyrazine, are heterocyclic compounds where their nitrogen heteroatoms are present at 1- and 4- positions [1,2]. These nitrogen atoms in quinoxaline impart basic properties to the structure, help in stabilizing ion radical species and are responsible for their physicochemical and biological properties [1,3]. Derivatives of quinoxaline possess unique properties like good resonance energy, dipole moment, light emission and absorption ability, lipophilicity, several Lipinski properties, etc [3,4]. Different synthetic quinoxaline and its derivatives also have broad applications in biological and medical arena owing to their therapeutic and bioactive properties like anti-microbial, anti-thrombotic, anti-oxidant, anti-neoplastic activities, etc. They are also effective against some metabolic conditions and chronic diseases like leishmania, cancer, diabetes, HIV, neurological disorders, etc [1,3–8].

Discovery of graphene in 2004 was a revolutionary footstep in scientific field as it can be profoundly considered as the future of nanotechnology [9]. Graphene, an allotrope of carbon, is nano sized one atom-thick single layer sp^2 carbon sheet tightly arranged in a two-dimensional hexagonal honeycomb lattice [10]. It could interact with different materials owing to its π-bonds, which are oriented out of the plane and have widespread double-sided surface [10,11]. Surface of graphene is often modified by doping with metals, non-covalent functionalization to improve its reactivity and biocompatibility [10,11]. Performance of metal-based nanomaterials can be enhanced upon integrating them with graphene as it can enhance the electron transfer with its metal counterpart owing to its high electrical conductivity and provide higher effective surface area for binding with the analyte [11–13]. Graphene nanoplatelets possess some defects in its structure which in turn acts as decent anchoring sites for the metal nanoparticles thereby imparting good optical properties to them [11]. Graphene nanoplatelets has been earlier used for modification of nanoparticles of Pt, Pd, Au, TiO$_2$, etc., as a sensing material for several biomolecules [11–16].

During the tumorigenesis and following cancer progression, glycosylation pattern of cell surface and secreted glycoproteins undergo several alterations and thus these glycoproteins are the major cancer biomarkers used for clinical purposes [17]. Prostate cancer is one of the major causes of death worldwide in men above the age of 50 y [18–20]. As cancer cell proliferation of prostate epithelia and initial growth of prostate cancer cells are androgen dependent processes, prostate specific antigen (PSA) gene gets activated as it is regulated by androgen receptor [21]. PSA is the first biomarker for prostate cancer approved by the U.S. Food and Drug Administration (FDA) and is considered as gold standard biomarker for early detection of prostate cancer as well as screening in asymptomatic patients, disease progression, response to treatment by cancer patients upon chemotherapy and monitoring its recurrence to prolong the life-span of patients [18,21–23]. In prostate cancer patients, PSA is highly expressed by malignant cells of the prostate gland and its level in serum gets elevated (>10.0 ng/mL) upon its secretion from the malignant prostate gland [18,22,24]. A total PSA level of lower than 4.0 ng/mL is considered as normal and negative of prostate cancer [19,20,25]. Several conventional techniques for PSA detection have been recognized using different methods like electrochemical immunoassay, differential pulse voltammetry (DPV), electrochemical impedance spectroscopy (EIS), enzyme-linked immune-absorbent assay (ELISA), chemiluminescence, etc [20,23,24,26–29]. However, most of these techniques are inconvenient for reasons like high time-labor-cost, low stability, need of special handling, use of expensive instruments and complex procedures and often lack selectivity [20]. Some optical methods like colorimetry, fluorescence, etc., are reported too for PSA detection but in most of the cases, biosensors are made up of enzymes/antibodies/aptamers as recognition and detection element to PSA [30–32]. Mostly used methods in medical practices are immunoassays

like ELISA which also involve use of antibodies. However, these techniques work on the principle of specific antigen-antibody interactions where costly enzymes/antibodies/aptamers are being used and eventually, price for the clinical detection of PSA upsurges. Thus, development of rapid, cost-effective, simple, antibody-free methods for PSA detection is of utmost importance [33–35].

Earlier PSA has been detected using different methods using biosensors made of metal nanoparticles (NP) like AuNP, AgNP, PdNP, PtNP, etc [19,24,27–29]. A fluorescent nanoprobe made up of graphene oxide quantum dots-silver nanocrystals conjugate was synthesized for the sensing of PSA with the help of anti-PSA antibody with a limit of detection (LOD) of 0.3 pg/mL [32]. Streptavidin coated EuNP has shown PSA sensing ability and deliver an LOD of 0.38 mg/L where PSA was biotinylated at first [36]. PSA has been detected using circular dichroism (CD) spectroscopy with Au@Ag nanorod dimer sensor which gives an LOD of 0.076 aM [37]. AuNP was used for PSA sensing using Surface-enhanced Raman scattering (SERS) methods as they have proved to be ideal candidates as SERS probes [38]. A SERS-based magnetic aptasensor made up of magnetic nanoparticles (MNP) core-(AuNPs) satellite assemblies were used to detect PSA with an LOD of 5.0 pg/mL [38]. Sensitive detection of PSA was carried out using AuNP in presence of antibody which provides an LOD of ~1 pg/mL in human serum [39]. Although they provide good sensitivity towards PSA detection, they are made of precious metals and might come up with the shortcoming of being uneconomical. Researchers have also used a sandwich ELISA method based on anti-PSA IgY antibody for the detection of PSA which delivers an LOD of 0.083 ng/mL [40]. Scientists have screened a number of phage monoclones and the phage monoclone expressing peptide TSIANYIGLALRA was used for specific detection of PSA using ELISA providing an LOD of 0.18 ng/mL [41].

Surface-enhanced Raman scattering (SERS) is a fast and sensitive technology with outstanding reproducibility for the detection of various molecules. It is a powerful vibrational spectroscopic method where inelastically scattered photons excite the vibrational energy levels of the sample and provide its molecular information, which can overcome the low sensitivity issues faced in typical Raman spectroscopy [38,42]. Ultrasensitive detections of several analytes could be achieved in presence of nanostructured metal surfaces using the hot electron spots on metal nanostructures, which are responsible for massive Raman enhancement of weak Raman signals of the analytes [43]. SERS has earlier been used for detecting biomolecules of patient samples and the matrix used was either tissue samples or other biofluids where the metal nanoparticles remain in close vicinity to the analyte [42,44]. In recent times, researchers have developed metallic nanoparticles like AuNP, AgNP for intracellular imaging using SERS, medical diagnosis of diseases like cancer was performed, in cases like liver biopsy, analysis of serum and urine samples for prostate, breast and bladder cancer, adenoviral conjunctivitis, brain injury diagnostic, etc., making it ideal for point-of-care tool [42,45,46].

In our present work, we aimed to synthesize iron-based nanocomposite using a quinoxaline derivative and further modify it with graphene nanoplatelets to find its yet unexplored application towards the sensing of cancer biomarker PSA. The graphene-based nanocomposite was characterized by several analytical methods and mechanism for its interaction with PSA was studied using fluorescence, Raman, circular dichroism (CD) spectroscopy and theoretical studies.

2. Experimental

2.1. Materials

All chemicals for the synthesis of 1d were procured from Sigma-Aldrich, Alfa-Aeser, Acros, whilst corresponding solvents were purchased from Rankem, Merck and Acros. Iron(III) nitrate nonahydrate and dextrose were obtained from Merck, India. Graphene nanoplatelets (Gr) (surface area 750 m^2/g) were purchased from Sigma-Aldrich, India.

Bilirubin was procured from HiMedia, India. Cholesterol was obtained from LOBA Chemie, India. Prostate specific antigen (PSA) was procured from Monobind Inc., USA. Ringer-Lactate solution (RL) (aqueous solution of sodium lactate, sodium chloride, potassium chloride, calcium chloride) and semisynthetic human insulins, namely, actrapid and huminsulin were purchased from local drugstore. Lyphochek Assayed Chemistry Control (Bio-Rad) was used as the source of lyophilized human serum as working material. Serum solution was reconstituted by following the directions given in the attached booklet. All the experiments were carried out using triple distilled water.

2.2. Instruments and apparatus

The UV–visible spectroscopic measurements were performed using a Hitachi model U-4150 UV–Vis-NIR spectrophotometer and a quartz cuvette of 1 cm path length was used as a sample holder. Steady-state fluorescence experiments were performed using a PerkinElmer LS-55 fluorescence spectrometer with a quartz cuvette of 1 cm path length and the slits with band passes at 5 nm for both excitation and emission channels. A JEOL JEM-2100F transmission electron microscope (TEM) with 200 kV electron source was used to get the TEM images and selected area electron diffraction (SAED) pattern of the synthesized nanocomposite. A Malvern Zetasizer Nano ZS instrument was used for zeta potential (ξ) measurements. Powder X-ray diffraction (PXRD) analysis were performed using a Rigaku SmartLab automatic high resolution multipurpose PC Controlled X-Ray diffractometer system with Cu anode as the source with K-α value of 1.54060 Å (current 40 mA, voltage 40 kV). Fourier Transform Infrared (FTIR) spectroscopic data was recorded using a PerkinElmer FTIR/FIR spectrometer (Frontier) in the range of 3500 cm^{-1} to 400 cm^{-1}. XPS measurements were carried out using a Kratos Axis Ultra DLD photoelectron spectrometer, operating with 120 W (10 mA, 12 kV) using monochromatic Al K-α X-ray source. The system was acquired over the area of 300 $\times$ 700 μm^2 approximately using a Hybrid mode comprising of magnetic immersion and electrostatic lenses. Pass energies for survey spectra and high-resolution scans were 160 eV (step sizes of 1 eV) and 40 eV (step sizes of 0.1 eV) respectively. In order to minimize charging of the sample surface, a magnetically confined charge compensation system with low energy electrons was used. The spectra were collected with a 90° take-off angle, during all analysis the vacuum within the system was better than 5 $\times$ 10^{-9} Torr. CasaXPS (v2.3.25) software was used for the data analysis and the data was fitted using Voigt-like functions (LA Line shape in CasaXPS). All data was quantified after subtraction of a Shirley type background, using modified Wagner sensitivity factors as provided by the instrument manufacturer [47]. Raman spectroscopic analyses were carried out using a Renishaw inVia Raman microscope with the help of a Leica DM2700 M confocal upright microscope system. A Malvern MicroCal PEAQ-ITC instrument was used to perform isothermal titration calorimetry (ITC) experiment using the MicroCal PEAQ-ITC Analysis Software. Jasco J-1500 circular dichroism spectrophotometer was used to perform circular dichroism spectroscopic analysis. A Labman digital ultrasonic cleaner (model: LMUC-2) was used to sonicate the nanocomposite solution and centrifugation of the said solution was done using a Remi Elektrotechnik Ltd R-4C instrument. A digital Mettler Toledo Seven Compact pH/ion meter was used to measure and adjust the pH of solutions. A BOD incubator shaker NOVA model: SHCI 10(D) was used to maintain the temperature at 313 $\pm$ 0.5 K.

2.3. Synthesis of the nanocomposite

The quinoxaline derivative 6-nitroquinoxaline-2,3-diamine (1d) was synthesized in laboratory using previously reported method [48]. Briefly, 4-nitro orthophenylenediamine was treated with diethyl oxalate in 4 N HCl under reflux to get 6- nitroquinoxaline-2,3(1H, 4H)-dione (compound a) which was again treated with excess of $POCl_3$ under reflux condition to form 2,3-dichloro-6-nitroquinoxaline (compound b).

Compound b was then treated with phenylmethanamine in presence of $CaCO_3$ at room temperature to get 3-chloro-6-nitroquinoxalin-2-amine (compound c). Compound 1d (Fig. 1) was finally achieved by Buchwald-Hartwig amination on compound c using $Pd_2(dba)_3$ as a catalyst, XPhos as ligand and Cs_2CO_3 as base in presence of 3-dimethyl-laminopropylamine. Thereafter, an easy, fast, safe and inexpensive process devoid of any harmful and/or costly chemicals was used for the synthesis of 1d mediated Fe(III) nanoparticles modified with graphene nanoplatelets. 1 mM methanolic solution of 1d was prepared and pH of the solution was adjusted to 2.1 mL of 50 mM solution of $Fe(NO_3)_3 \cdot 9H_2O$ was added to an equal volume of 1 mM solution of 1d in a dropwise manner. To this mixture, 0.5 mg of graphene nanoplatelets was added, shaken for 5 min and then kept to settle at (313 $\pm$ 0.5) K. After 24 h of settling, the blackish-orange colored fine particles were precipitated out at the bottom of the reaction vial suggesting the formation of the nanocomposite. The solution was then dried under IR lamp to get the desired nanocomposite 1d-Fe-Gr. To get rid of any unreacted reagents, the obtained 1d-Fe-Gr was further washed with 50% methanolic solution for several times. For comparison, pristine 1d-Fe nanocomposite was also prepared by following the same synthesis procedure only without the addition of graphene nanoplatelets into the reaction medium. Working nanocomposite 1d-Fe-Gr solution was prepared by adding ~1 mg of 1d-Fe-Gr in 3 mL of water. The 1d-Fe-Gr solution was ultra-sonicated for 30 min at room temperature (298 $\pm$ 1 K) prior to each experiment for homogeneous dispersion of the nanocomposite in the solution.

2.4. Characterization of the nanocomposite

The solutions containing nanocomposites were first sonicated for 30 min at room temperature (298 $\pm$ 1 K) and then subjected to centrifugation for 10 min at 2500 rpm to get the supernatants. To know the physical morphologies like shape, size, roughness and dispersive nature of the nanocomposites, a drop from the supernatants was casted on a carbon-coated copper grid and used for TEM measurements. Zeta potential (ξ) measurement was carried out using the same supernatant to determine the charge developed between the solid 1d-Fe-Gr and the liquid medium. The measurements give the idea of stability of 1d-Fe-Gr in fluid suspension. PXRD, XPS and FTIR analysis were performed with the dried solid nanocomposites. A pinch of each nanocomposite was blended with dry KBr using a mortar-pestle and KBr pellet of the nanocomposites were prepared with the help of a hydraulic press. To know the presence of vibrational frequencies of the potential associations of the functional groups on the surface of the nanocomposites, FTIR analysis of the nanocomposites were carried out. Solid powder sample of the nanocomposites were placed in a grooved rectangular glass holder and PXRD analysis were performed to know their crystallographic structure. To know the elemental composition and their corresponding chemical and electronic states, XPS analysis of 1d-Fe-Gr was further carried out. Raman spectroscopy of the nanocomposites were carried out to know the changes in bond vibrations upon modifications.
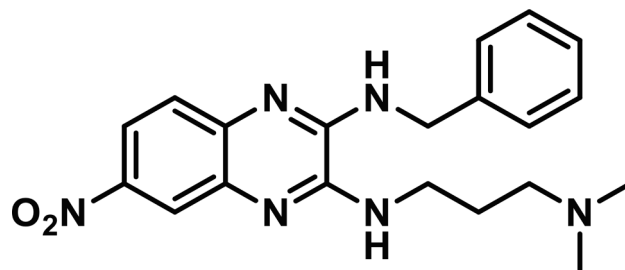

Fig. 1. Structure of quinoxaline derivative 6-nitroquinoxaline-2,3- diamine (1d).

2.5. Isothermal titration calorimetry

Isothermal titration calorimetry (ITC) experiment was performed to quantify the binding affinity (measured by the equilibrium dissociation constant (K_D)), binding stoichiometry (N) and calculate the corresponding thermodynamic parameters of the interaction of the metal-macromolecule complex (Fe(III) and 1d) using the following equation,

$$\Delta G = \Delta H - T\Delta S \tag{1}$$

where ΔG is Gibbs free energy, ΔH is the change in enthalpy, ΔS is the change in entropy and T is the absolute temperature. This gives the idea of entropic (ΔS) or enthalpic (ΔH) nature of interaction along with the binding stoichiometry. All the calorimetric experiments were carried out at room temperature (298 ± 1 K). A total of 19 serial injections, each containing 1 µL of 1d solution (1 mM) were transferred into the cell containing 150 µL of Fe(III) (5 mM). The syringe was stirred at a speed of 750 rpm and a gap of 150 s was maintained between two successive injections.

2.6. Sensing of cancer biomarker PSA by the nanocomposite containing solution

2.6.1. UV–Vis absorption spectroscopy

In order to investigate the interaction between the 1d-Fe-Gr and PSA, UV–visible absorption spectroscopy was performed at 298 ± 1 K. To keep the reaction conditions at per with biological relevance for clinical applicability, each set of experiments was carried out in serum medium. As the working medium for all sets of experiments, the reconstituted serum was used which was again 1000-folds diluted with RL to attain physiological significance. In order to sense PSA by 1d-Fe-Gr, 0.20 mL of the 1d-Fe-Gr solution (0.33 mg/mL) was first added to 1.80 mL of the working serum medium and then known aliquots of PSA (0.5 ng/mL) were successively added to this mixture and their corresponding absorbance were recorded at the λ_{max} 280 nm. A similar set was prepared in absence of 1d-Fe-Gr and taken as control. The rate of change in absorption intensities of PSA in presence of 1d-Fe-Gr were compared with the control experiment. Sensing assays were further performed in presence of high concentrations (higher than normal physiological limits) of biomolecules viz., glucose, cholesterol, bilirubin, actrapid and huminsulin which causes different comorbidities like diabetes, hypercholesterolemia, hepatic disorder and hyperinsulinemia respectively. Individual effects of these interfering biomolecules on PSA sensing by the 1d-Fe-Gr were further checked. To carry out the said simulations, dextrose and cholesterol (final concentration 10 µM each) and bilirubin (final concentration 45 µM) were added to the working serum medium and their corresponding absorbance spectra were monitored both in presence and absence of the 1d-Fe-Gr. Elevated concentration of insulin is observed in patients with high-risk prostate cancer (hyperinsulinemia) as insulin plays an important role in promoting cell growth and proliferation of prostate cancer cells and receptors [49–51]. Thus, influence of insulin (actrapid and huminsulin) on PSA sensing by 1d-Fe-Gr was monitored additionally. For that purpose, each of actrapid and huminsulin were added to the working serum medium keeping their final concentration 4 µIU/mL and sensing assays were carried out. As insulin and glucose are directly associated with each other, combined effect of these two biomolecules were also checked. Actrapid or huminsulin (final concentration 4 µIU/mL) and dextrose (final concentration 10 µM) in the working serum medium was added and their corresponding spectra were taken both in presence and absence of the 1d-Fe-Gr. The final spectra recorded were the average of three runs. Limit of detection (LOD) and limit of quantification (LOQ) of PSA were calculated using this UV–visible spectrophotometric method. LOD and LOQ were calculated using the following equations with the help of slope (S) and standard deviation (σ) of the calibration curve of the responses.

$$LOD = 3.3 \, (\sigma/S) \tag{2}$$

$$LOQ = 10 \, (\sigma/S) \tag{3}$$

2.6.2. Raman spectroscopic analysis

Raman spectroscopy is a powerful analytical tool for characterization of carbon-based materials. To know the chemical structures of 1d-Fe and 1d-Fe-Gr, few drops of their respective solutions were casted on an Al-foil wrapped glass slide to make a thin layer in order to perform the Raman spectroscopic analysis. Both 1d-Fe and 1d-Fe-Gr were then compared with pristine 1d and pristine graphene nanoplatelets to compare the changes in bond vibrations upon modification. Measurements were taken in the range of 3200 cm^{-1} to 50 cm^{-1} using 785 nm of solid-state laser excitation (using 0.1% of 300 mW power, 50X objective lens, 0.5 numerical aperture, 50 s exposure time) to find their characteristic peaks. In order to investigate the mechanism of interaction between 1d-Fe-Gr and PSA, Raman spectra of 1d-Fe-Gr solution with varying concentration of PSA (0.34 pg/mL to 1.50 pg/mL) in serum medium were also taken. Raman spectra of varying concentrations of other cancer biomarkers (CA 19-9 for pancreatic cancer and CEA for colorectal cancer) were also taken in presence of 1d-Fe-Gr in serum medium to understand its specificity towards PSA.

2.7. Fluorescence spectroscopy

The fluorescence intensity of PSA (0.5 ng/mL) in working serum medium was recorded at the emission maximum of 345 nm (intrinsic fluorescence of proteins due to tryptophan and tyrosine residues in PSA) upon excitation at 290 nm as control. Then, different aliquots of the solution containing 1 mg/mL of 1d-Fe-Gr were added successively to PSA (0.5 ng/mL) to study its interaction with the biomarker. Working medium as explained above in section 2.6.1 was used as reference blank for each experiment. The quenching of the intrinsic fluorescence of PSA by 1d-Fe-Gr was analyzed using the Stern-Volmer equation both in absence and presence of high concentration of biomolecules like glucose and cholesterol to mimic the pathophysiological conditions at room temperature (298 ± 1 K).

$$F_0/F = 1 + K_{SV} \, [Q] \tag{4}$$

where, F_0 and F are the relative fluorescence intensities of PSA at 345 nm in absence and presence of the quencher (1d-Fe-Gr) respectively and [Q] is the concentration of the quencher (1d-Fe-Gr). The slope of the plot of F_0/F vs. [Q] gives the value of Stern-Volmer quenching constant K_{SV}.

2.8. Circular dichroism spectroscopy

Circular dichroism (CD) spectroscopic analysis was performed in order to determine conformational changes (if any) in the native structure of protein upon binding with the 1d-Fe-Gr. To study the selective interaction between the 1d-Fe-Gr and PSA, CD spectra of PSA along with other cancer biomarkers CA 19-9 and CEA were recorded both in presence and absence of the 1d-Fe-Gr in the serum medium. Final spectra were taken as the average of three runs and the CD results were expressed in terms of mean residual ellipticity (MRE) at 222 nm using the following equation [35].

$$[\vartheta\lambda] = \frac{\mu\vartheta}{10LC} \tag{5}$$

where C is the molar concentration of the proteins, L is the path length of the cuvette (0.1 cm), θ is the observed rotation, µ is the mean residual weight of the proteins. Using the MRE values at 222 nm, the α-helical contents of the said proteins both in presence and absence of the 1d-Fe-Gr were calculated using the following equation [52].

$$\alpha\_helix\,(\%) = \frac{[-MRE + 2340]}{-30300} \qquad (6)$$

2.9. Theoretical studies

Molecular docking studies were carried out to find out the mode of interaction of 1d-Fe-Gr with the protein biomarker PSA. The amino acid sequence of PSA (PDB ID: 2ZCH) was taken from Protein Data Bank (PDB) structural data base. Hex 8.0.0 docking software was used to obtain the energy minimization models of the interaction between 1d-Fe-Gr and PSA and the docked pose was visualized and analyzed using molecular visualization system PyMOL.

3. Results and discussion:

3.1. TEM analysis

The TEM micrographs of 1d reveal its nano dimensional nature with spherical shape and the average size of the particle is 10–20 nm (Fig. S1a). However, upon interaction of 1d with Fe(III), a distinct needle shaped nanocomposite is formed and the size of the 1d-Fe complex keeps on growing to the average size of 80–90 nm in length and 15 nm in breadth (Fig. S1b). Remarkably, in presence of graphene nanoplatelets, size of the newly synthesized nanocomposite (1d-Fe-Gr) decreases drastically compared to its pristine version (1d-Fe) while retaining its original needle like shape (Fig. 2a). The average particle size of 1d-Fe-Gr is 30–40 nm in length and 2–10 nm in breadth. This might be due to the fact that during the synthesis of 1d-Fe-Gr, spherical shaped graphene nanoplatelets with average size of 20 nm as obtained from its TEM image (Fig. S1c) gets deposited on the surface of 1d-Fe nanoparticles as seen in Fig. 2a and hinders the large growth of the particles and thereby generates the nanocomposite (1d-Fe-Gr) with controlled growth. Presence of graphene nanoplatelets plays a massive role in reducing the size of the nanocomposite to a great extent and facilitates the generation of larger effective surface area. Thus, 1d-Fe-Gr could bind with the analyte PSA to a higher extent compared to 1d-Fe alone as reflected from UV–visible spectroscopic data (section 3.10). SAED pattern of the 1d-Fe-Gr (Fig. 2b) shows the presence of bright concentric rings which illustrates the polycrystalline nature of the 1d-Fe-Gr. The rings were then analyzed with the help of ImageJ software

(version 1.8.0_172) and their corresponding (hkl) planes were assigned after comparing with the PXRD analysis data (discussed in section 3.3). Fig. 2c shows the presence of lattice fringes in 1d-Fe-Gr with an interlayer spacing (d-spacing) of 2.80 Å at its corresponding (031) plane. Narrow particle size distribution with size 33–38 nm could be seen from particle size histogram (Fig. 2d). Elemental analysis of 1d-Fe-Gr using energy-dispersive X-ray spectroscopy (EDX) as shown in Fig. 2e clearly indicates the presence of Fe and C in the nanoparticles.

3.2. Zeta potential

Determination of zeta potential is significant for the characterization of the nanocomposite to understand its colloidal stability in suspension by determining its electrostatic potential at the electrical double layer surrounding it in solution. Zeta potential values beyond the range 10 mV to 10 mV of the nanocomposite indicates that it is electrically stabilized and sterically protected to a good extent and are less prone to agglomerate rapidly as electrostatic repulsion predominates [53]. The magnitude of the ζ potential value of 1d is very less (a small positive ζ potential value of 0.607 mV due to slight protonation of the secondary amine groups at pH 2) which indicates its lesser stability in the colloidal state and higher tendency of agglomeration (Table 1). On the other hand, a decent positive ζ potential value of 19.8 mV is observed for 1d-Fe which appears due to complexation of 1d with positively charged metal ion. The surface charge reverses with a negative zeta potential value of -17.0 mV upon incorporation of graphene in 1d-Fe-Gr which accounts for its good stability in the colloidal state and less tendency of agglomeration. This also agrees with TEM micrographs which shows smaller size of 1d-Fe-Gr. The negative ζ potential in 1d-Fe-Gr is due to the presence of graphene nanoplatelets (which itself has a ζ potential of -26.6 mV) in the system as it is placed on the surface of 1d-Fe and

Table 1
ζ potential values of 1d and prepared nanocomposites.

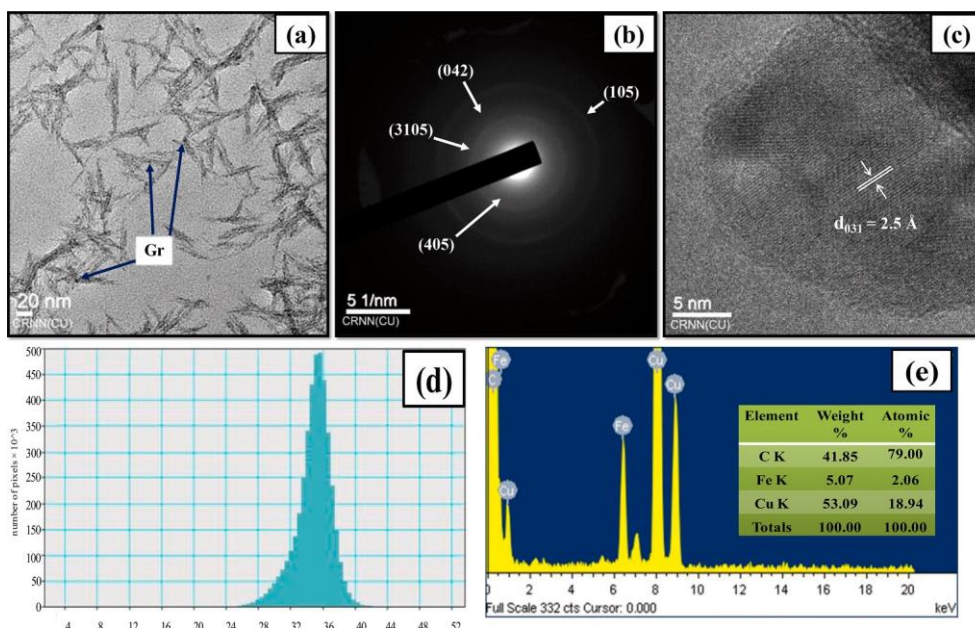| Variation	Zeta potential (mV)
1d	0.607
1d-Fe	19.8
1d-Fe-Gr	—17.0
Gr	—26.6

Fig. 2. (a) TEM image, (b) SAED pattern, (c) lattice fringes, (d) histogram, (e) EDX spectrum (inset shows elemental percentages) of 1d-Fe-Gr.

provides an electron rich medium and thus imparts a negative zeta potential value.

3.3. PXRD analysis

Powder X-ray diffraction pattern of 1d and 1d-Fe-Gr (Fig. 3) shows the occurrence of a handful of sharp peaks which validates the presence of periodic crystal lattice in the powder form of both of them. The peak positions obtained from the diffraction patterns were then tallied with the database obtained from the Joint Committee on Powder Diffraction Standards (JCPDS). PXRD data with possible (*hkl*) planes and corresponding JCPDS numbers are summarized in Table S1. Fig. 3 shows that the most intense peaks come from 2θ values of 7.920°, 11.282°, 17.301°, 20.025°, 20.901°, 23.140°, 26.759° corresponding to (101), (011), (001), (020), (102), (004), (11), (041), (122), (221) planes respectively in case of 1d. From this data, it could be said that lattice structure of 1d is mostly primitive with monoclinic system. Also, presence of end-centered lattice is also seen. Upon its modification with Fe(III) and graphene nanoplatelets, change in diffraction pattern as well as appearance of different new peaks are observed in the diffraction pattern of the product 1d-Fe-Gr. This suggests its change in lattice system compared to pristine 1d along with the introduction of a new lattice system. The lattice structure of 1d-Fe-Gr is mostly primitive. In contrast to 1d, a new body-centred lattice is also observed here alongside end-centred one with monoclinic system. Major diffractions appear due to 2θ values of 15.708°, 19.533°, 21.106°, 30.083°, 36.920°, 40.685°, 43.324° which corresponds to (011), (210), (311), (611), (141), (251), (134), (22) respectively. Presence of orthorhombic system is also seen. The interlayer crystallographic lattice plane distance (*d*-spacing values) obtained from PXRD data using Bragg's equation matches well with that of the values obtained from SAED pattern of 1d-Fe-Gr using ImageJ software. It is interesting to see that the peaks in 1d-Fe-Gr appear at higher angles, which suggest smaller interplanar distances for crystal
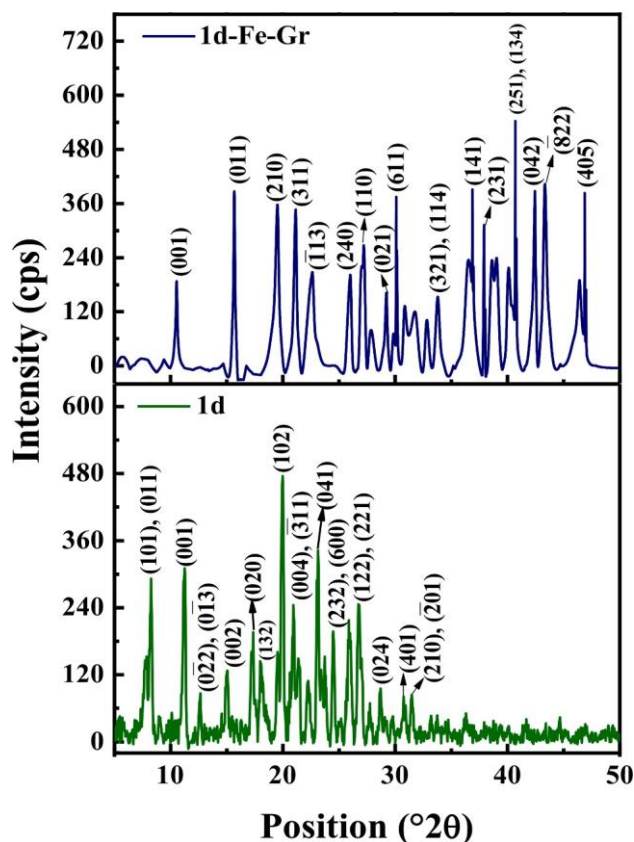
planes or d-spacing value and the diffraction peaks have relatively high intensity which accounts for greater lattice growth compared to 1d. The lattice parameters in 1d-Fe-Gr appear due to the interactions of molecules in the lattice owing to 1d and Fe(III) and further interaction with graphene nanoplatelets.

3.4. FTIR spectroscopy

Fig. 4 shows the FTIR spectra of 1d, 1d-Fe and 1d-Fe-Gr particles and the possible functionalities are listed in Table S2. It could be seen that peak position at 3416 cm^{-1} appearing due to N–H stretching in 1d disappears in both 1d-Fe and 1d-Fe-Gr upon its modification which suggests the possibility of N atoms of 1d to interact with Fe atoms. A strong peak at 1337 cm^{-1} appears due to C–H bending of –CH$_3$ group in 1d which shifts to 1387 cm^{-1} in both 1d-Fe and 1d-Fe-Gr [54]. This suggests that the C–H bond gets stronger which in turn suggests shortening in bond length of C–H [55]. This might be due to the possible interaction of N atoms of 1d attached to –CH$_3$ group with Fe atoms. In 1d-Fe system, appearance of broad peak around 698 cm^{-1} indicates Fe-O stretching [56]. Electron donor atoms like nitrogen and oxygen in 1d can bind efficiently with Fe atoms which has vacant d-orbital in its electronic configuration. However, extent of interaction of 1d with Fe atoms intensifies in presence of graphene nanoplatelets. Appearance of peaks at 627, 611, 586, 475, 444 cm^{-1} in 1d-Fe-Gr confirms the formation of α-Fe$_2$O$_3$ upon the interaction between 1d and Fe atoms in presence of graphene nanoplatelets which are now more exposed towards its surface [57–59].

3.5. Raman spectral analysis

The Raman spectral analysis shows the characteristic peaks of 1d due to the presence of different bonds listed in Table S3. Presence of characteristic peaks of graphene nanoplatelets at 1306 cm^{-1}, 1581 cm^{-1} and 2610 cm^{-1} appear due to D band (disorder band) owing to out of plane ring breathing mode of sp^2 atoms, G band (graphite band) due to intraplanar stretching modes of the strongly connected σ-bonded carbons as well as bond stretching of the pairs of sp^2 carbon atoms and 2D or G' (second-order disorder band) due to second-order overtone of a different in-plane vibration respectively (Fig. 5) [60–62]. Upon the interaction between 1d and Fe(III), characteristic peaks of 1d disappears suggesting their possible involvement in the formation of the 1d-Fe complex where distinctive peaks of α-Fe$_2$O$_3$ also appears in the region of 226 cm^{-1} to 612 cm^{-1} which matches well with the literature [63–64]. The presence of α-Fe$_2$O$_3$ was also indicated by the FTIR spectroscopy. However, the characteristic peaks of graphene nanoplatelets get blue shifted towards higher wavenumber (1306 cm^{-1} to 1311 cm^{-1} in D band, 1581 cm^{-1} to 1597 cm^{-1} in G band and 2610 cm^{-1} to 2624 cm^{-1} in 2D or G') in 1d-Fe-Gr which suggests shortening of sp^2 hybridized C–C bond length in graphene nanoplatelets due to the strain induced by 1d-Fe. It could be due to the fact that upon introduction of 1d-Fe system in graphene nanoplatelets, Fermi level of the latter could change due to its charge transfer to 1d-Fe system. Also, the laser used for the Raman experiment (785 nm) could excite the surface plasmon of 1d-Fe system and hot electrons could arise from the decay of surface plasmon of 1d-Fe system which may account for electron cloud transfer from 1d-Fe to graphene nanoplatelets. As a result, charge redistribution could take place in 1d-Fe-Gr system and different charges could be localized on 1d-Fe and its surrounding graphene nanoplatelets surface [65]. Thus, electrostatic attractive force between 1d-Fe and graphene nanoplatelets and electrostatic repulsive force in the locally charged graphene nanoplatelets would cause a local strain between graphene nanoplatelets and the metal nanoparticle. Formation of this local strain might be the cause of limited growth of 1d-Fe on graphene nanoplatelets surface as also observed in TEM images discussed in section 3.1 and ζ potential studies discussed in section 3.2. The major peaks of 1d-Fe complex diminish to a great extent, which suggests strong interaction of 1d-Fe complex with
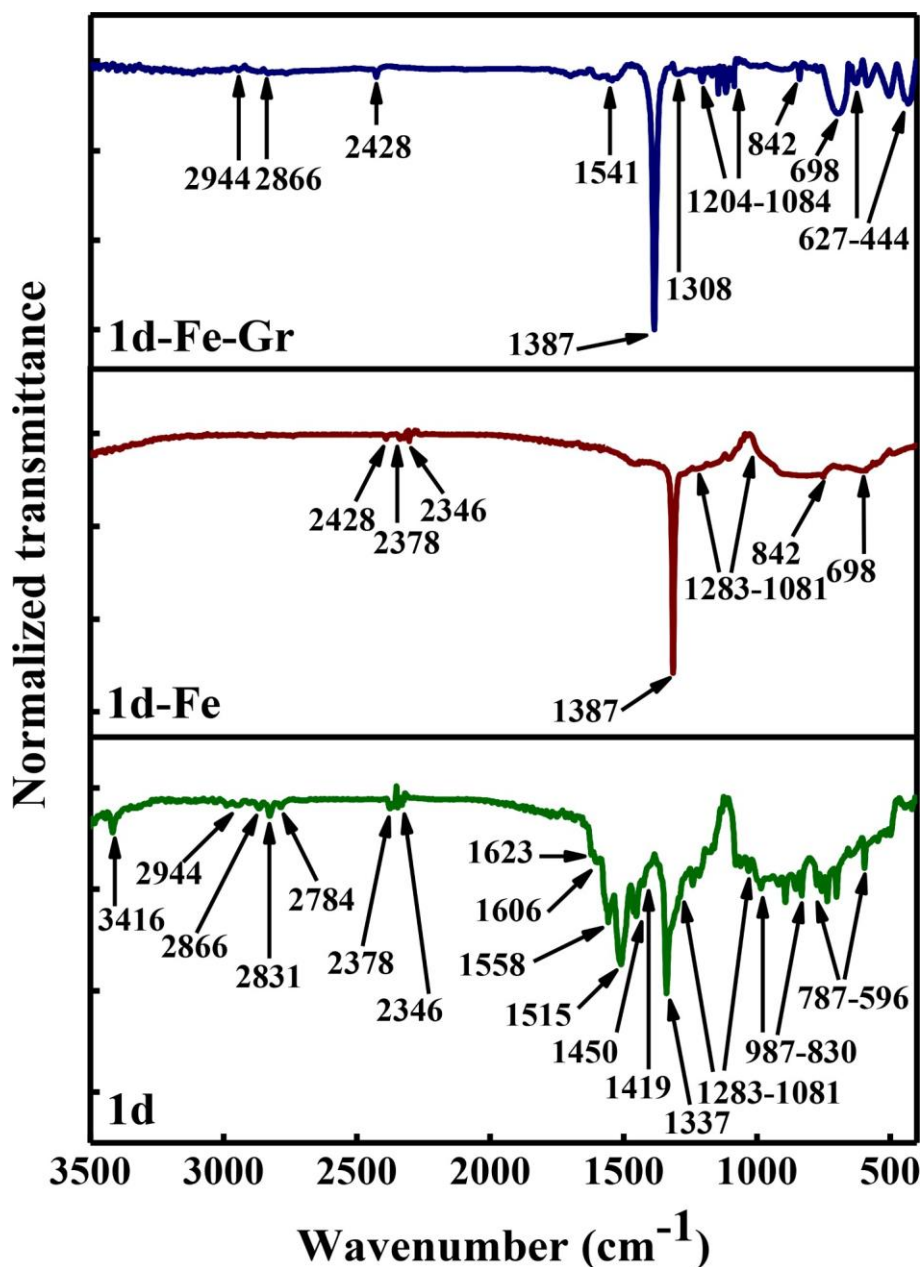

Fig. 3. PXRD patterns of 1d (green) and 1d-Fe-Gr (blue).

Fig. 4. FTIR spectra of 1d (green), 1d-Fe (red), 1d-Fe-Gr (blue).

graphene nanoplatelets and structural orientation of 1d-Fe in presence of graphene nanoplatelets. Peaks of graphene nanoplatelets intensify because it is situated on the surface of 1d-Fe complex which could also be seen from the TEM micrographs. The integrated intensity ratio of D and G bands (I_D/I_G) is used to determine the intralayer disorder or defect population in graphitic materials where a high I_D/I_G ratio indicates more defects in graphene nanoplatelets' surface [66–68]. I_D/I_G ratio increases from 1.82 to 1.95 from pristine graphene nanoplatelets to 1d-Fe-Gr which suggests increase in defect as more sp^2 domains are formed and thus PSA can approach more easily to the 1d-Fe-Gr and bind with it to a greater extent.

3.6. XPS analysis

X-ray photoelectron spectroscopic (XPS) analysis of the 1d-Fe-Gr material reveals a rich surface chemistry for carbon, oxygen and nitrogen, whilst iron is present as Fe_2O_3-like material, give the Fe($2p_{3/2}$)

binding energy of 711.5 eV and a broad satellite structure at *ca.* 719.5 eV. The carbon and oxygen core-level spectra reveal signals attributable to CC/CH, C-N, C-O, Fe-O, -OH and CO_x/NO_x species.

The N(1s) spectrum reveals a range of nitrogen chemical states, with binding energies of 339.3 (red peak), 401.2 (green), 403.3 (blue) and 407.1 eV (lilac). If we consider the 1d material then there are three significantly different nitrogen environments, specifically the N-CH₃/-CNH-, aromatic N and NO₂ functions. Typical binding energies for these are in the range of 399 – 401 eV for aromatic and N-C functions and 406–408 eV for NO$_x$ species [69]. From the structure of the 1d material (Fig. 1), we would expect a ratio of approximately 3:2:1 for C-N, aromatic N and NO₂ respectively. However, based on spectral intensities alone, it is clear this ratio is different for the composite material.

The N(1s) species at *ca.* 407 eV is higher in binding energy than that expected for NO₂ and more like that of NO₃, suggesting bonding between the NO₂ and oxide surface, forming a nitrate, this is supported by the O/N ratio of 3.3 for the 407 eV peak to the O(1s) signal at 533.2 eV
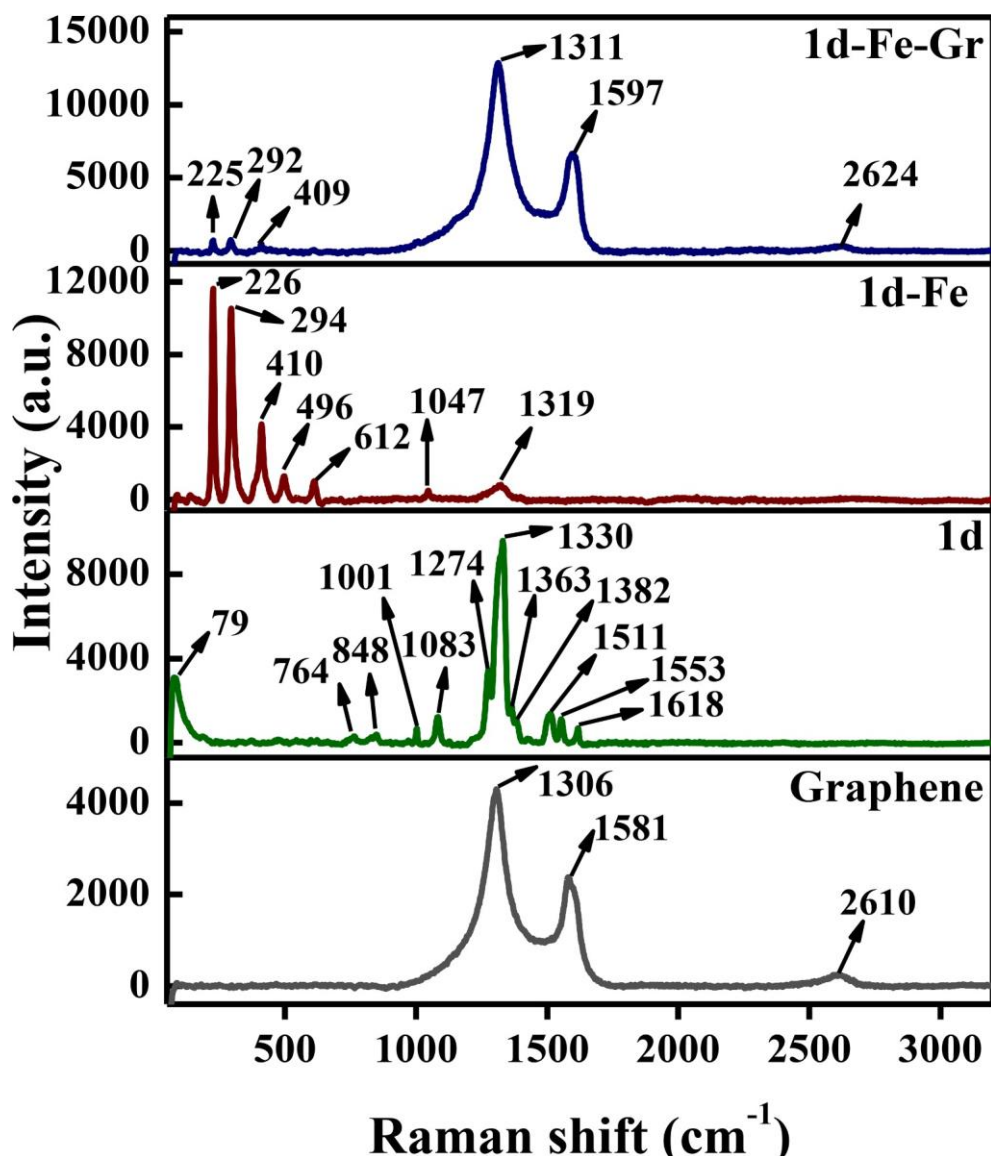
Fig. 5. Raman spectra of graphene nanoplatelets (grey), 1d (green), 1d-Fe (red), 1d-Fe-Gr (blue).

(blue peak in Fig. 6(c)) which is attributed to the oxygen in nitrates, the slight difference we attribute to uncertainty in the photoelectron background signal, shake-up structure on which the 407 eV peak is superimposed or some unreacted NO_2 moieties which may indicate a small amount of materials binds in a different way [69]. The N(1s) signals at 399.3 and 401.2 eV are in the expected 3:2 ratio, whereas the small blue peak at *ca.* 403 eV (<3% of the total concentration) may be attributed to a small amount of protonation or further nitrogen shake-up structure. Unexpectedly the ratio of the nitrate signal to the other nitrogen species is approximately 3:2:12.

3.7. ITC measurements

ITC data was obtained by titrating 1d (1 mM) with Fe(III) (5 mM) solution and the corresponding data was fitted using one set of sites model (Fig. 7). The thermodynamic parameters for the titration are listed in Table 2. Negative ΔG value (—4.18 kcal/mol) suggests that the binding of Fe(III) to 1d is a spontaneous and favorable process. ΔH value (—80 kcal/mol) indicates that the interaction between 1d and Fe(III) is exothermic. Small equilibrium dissociation constant (K_D) value (8.6 $\times$ 10^{-4}M) suggests greater binding affinity of the ligand (1d) to the metal

(Fe(III)). However, it is interesting to observe that binding stoichiometry (N) of the interaction between 1d (1 mM) and Fe(III) is high, i.e., four atoms of Fe(III) can bind with one molecule of 1d. However, if the structure of 1d is considered, binding of its one molecule with four Fe (III) atoms seems less likely to happen. This could be attributed due to the fact that 1d itself is nano-dimensional (average particle size 10–20 nm as observed from TEM images). It has a spongy texture with several porous sites which are rich in electrons. Upon the introduction of Fe(III) into the system, the metal here acts as a guest and some rearrangements in the structure of host 1d takes place. Fe(III) now has a wide access over 1d and keeps on binding with it through the electron rich anchoring sites and forms an extended woven structure which might result in higher number of binding sites in 1d available for Fe(III). However, 1d-Fe-Gr synthesized using 1 mM 1d solution and 50 mM $Fe(NO_3)_3 \cdot 9H_2O$ solution keeping 1d: Fe(III) = 4.4 as suggested from ITC data was not able to sense PSA (LOD 6.537 pg/mL). However, sensing was observed only when 1d and Fe(III) were present in 1:1 ratio.

3.8. Limit of detection (LOD)

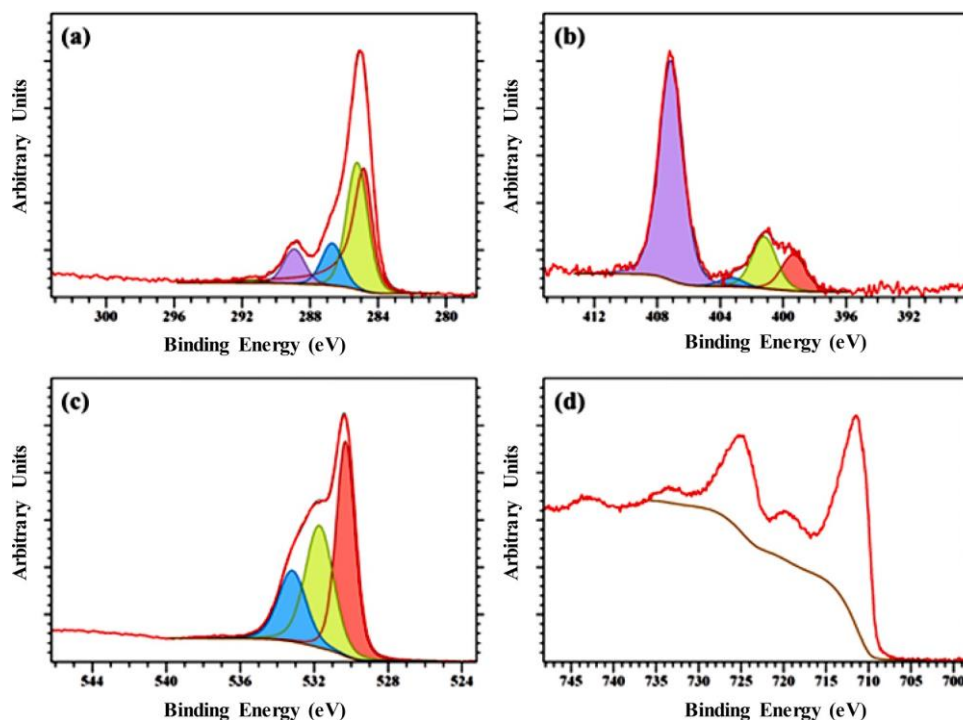The sensing methods should be highly accurate, sensitive and

Fig. 6. (a) C(1s), (b) N(1s), (c) O(1s) and (d) Fe(2p) core-level spectra for 1d-Fe-Gr sample.

selective as concentrations of the cancer biomarkers are low at an early stage of cancer. It is also important to avoid false positive test results and corresponding overtreatment.

3.8.1. UV–visible spectroscopic analysis

Spectrophotometric experiments were performed at the wavelength 280 nm to determine the interaction between PSA and 1d-Fe-Gr. Control experiments were performed by gradually adding PSA to the cuvette containing working serum medium and subsequent absorption intensities were recorded which increases with increasing PSA concentration. In presence of pathophysiological condition causing biomolecules like dextrose, cholesterol, bilirubin, actrapid and huminsulin in the working serum medium, similar change in absorption intensities of PSA were observed. The said simulations were further carried out with 1d-Fe-Gr in serum medium. It was observed that the rate of increase in absorption intensities of PSA enhanced largely in presence of 1d-Fe-Gr as spectral changes of PSA are much more prominent compared to the control set (Fig. 8). Calculated LOD values of PSA in each condition sets (Table 3) show that the 1d-Fe-Gr was able to sense PSA to a considerable extent as it offers high signal enhancement with high slope values.

Nonetheless, in presence of various physiological variables like dextrose, cholesterol, bilirubin, actrapid and huminsulin, LOD value of PSA further rises substantially in control solutions. This may cause difficulties in timely detection of PSA in serum. But results show that their presence does not interfere with PSA sensing using 1d-Fe-Gr. In fact, significant improvement in detection threshold was achieved in serum medium in presence of glucose, cholesterol, bilirubin, actrapid and huminsulin as the LOD obtained is much less as compared to an otherwise healthy condition. Thus, this detection method could also be applied efficiently to the patients suffering from comorbidities like diabetes, hypercholesterolemia and hepatic disorders. However, even if the patient serum sample does not contain any of these physiochemical entities, detection of PSA with even lower LOD could still be accomplished efficiently by 1d-Fe-Gr by the external addition of them in the patient serum. Table S4 shows different analytical parameters associated

with PSA sensing by the 1d-Fe-Gr along with their correlation coefficient (R^2). Fig. 8 shows absorption spectra for PSA sensing at different condition sets while Figure S2 shows their respective calibration plots.

3.8.2. Detection of PSA by surface enhanced Raman scattering (SERS) using 1d-Fe-Gr as a reporter

Upon its contact with PSA, characteristic Raman spectral peaks of 1d-Fe-Gr at 1311 cm^{-1}, 1597 cm^{-1} and 2610 cm^{-1} get shifted to 1314 cm^{-1}, 1600 cm^{-1} and 2618 cm^{-1} respectively which suggests strong interactions between them. However, PSA was able to enhance the Raman signal of 1d-Fe-Gr as the Raman signal intensities of the bands of 1d-Fe-Gr at 1314 cm^{-1} and 1600 cm^{-1} intensified with the increase in concentration of PSA as a greater number of PSA molecules can interact with 1d-Fe-Gr (Fig. 9). This could occur due to electric field enhancement due to surface plasmon of 1d-Fe-Gr and charge transfer between 1d-Fe-Gr and PSA as already described in section 3.5. However, it is noteworthy to mention that no shift in peak position of graphene nanoplatelets is observed in presence of PSA which suggests PSA has no interaction towards graphene nanoplatelets alone but with 1d-Fe-Gr exclusively (Fig. 9 inset). Linear relationship between Raman spectral intensity and PSA concentration could be seen from the Fig. 10. An attractive limit of detection value of 0.410 pg/mL was observed using this technique for PSA detection. Similar spectral correlations were not observed for other cancer biomarkers like, CA 19-9 and CEA.

3.9. Specificity of 1d-Fe-Gr towards PSA sensing using absorption spectroscopy

To confirm the specificity of the developed method, synthesized 1d-Fe-Gr was also used to sense CA 19-9 and CEA using absorption spectroscopy (biomarkers for pancreatic and colorectal cancers respectively) in serum by keeping all the experimental conditions alike. However, 1d-Fe-Gr failed to detect both the biomarkers in presence and absence of any bio-analytes. 1d-Fe-Gr could not lower the LOD values below their control value in serum and their corresponding LOD values exceeded the range of their physiological concentration in serum (Tables 4-5). Again,
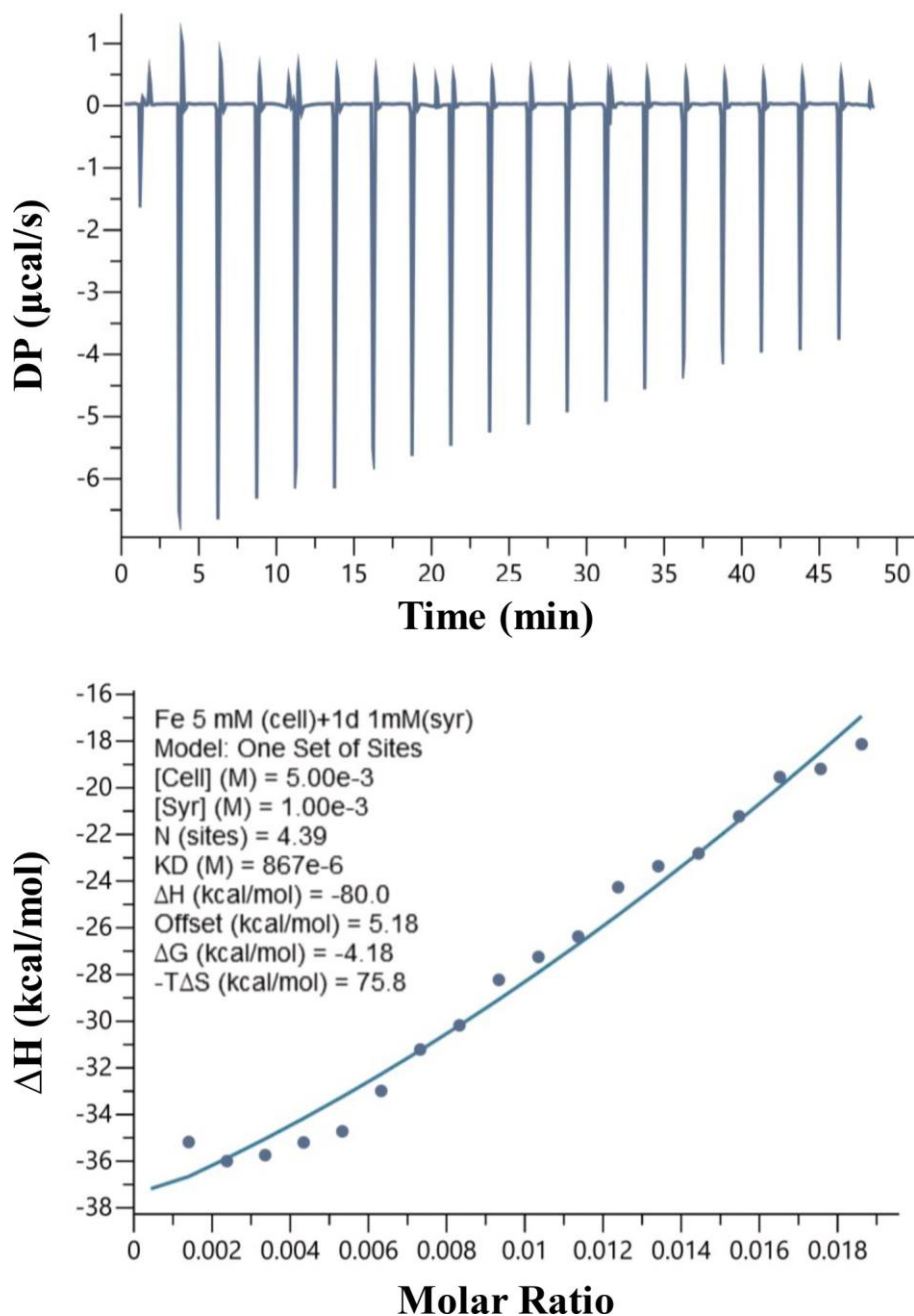
Fig. 7. ITC results of interaction between 1d and Fe(III).

Table 2

Summary of affinity measurements of the interaction between 1d (1 mM) and Fe (III) (5 mM).

N (sites)	K_D (M)	ΔH (kcal/mol)	-TΔS (kcal/mol)	ΔG (kcal/mol)
4.39	8.67×10^{-4}	—80.0	75.8	—4.18

Raman spectroscopic analysis also verifies that no significant change in Raman spectra of 1d-Fe-Gr (neither in change in intensity nor in shift in peak positions) has occurred in presence of CA 19-9 and CEA. This verifies that the 1d-Fe-Gr has good specificity in sensing CA 19-9 and there could not be as much of chance for a false positive result.

In order to find out the specificity of the designed nanocomposite, different combinations of the nanocomposites were used to sense PSA in serum (Table 6). It is worthwhile to mention that all the other combinations of the nanocomposites were unable to sense PSA in serum medium beyond its control value in similar experimental set-up. This confirms that graphene nanoplatelets play the key role in imparting new properties to 1d-Fe-Gr and provides sensing ability to the nano-composite (1d-Fe) which does not show any sensing properties towards PSA otherwise. It might be due to the fact that 1d-Fe compared to 1d-Fe-Gr for the detection of PSA as it has high affinity towards PSA as compared to 1d-Fe alone while their corresponding LOD values drop from 17.619 pg/mL to 0.879 pg/mL. It could be due to high electron mobility of graphene nanoplatelets present on the nanocomposite sur-face which is responsible for the electron transfer with its metal coun-terpart (Fe(III)) and boosted up the vicinity of the nanocomposite thereby enhancing its sensing performance. Also, it provides higher effective surface area owing to its wide 2D space around 1d-Fe-Gr for better binding with PSA which also has an extended structure. Graphene nanoplatelets possess some defects in its structure (appearance of sharp
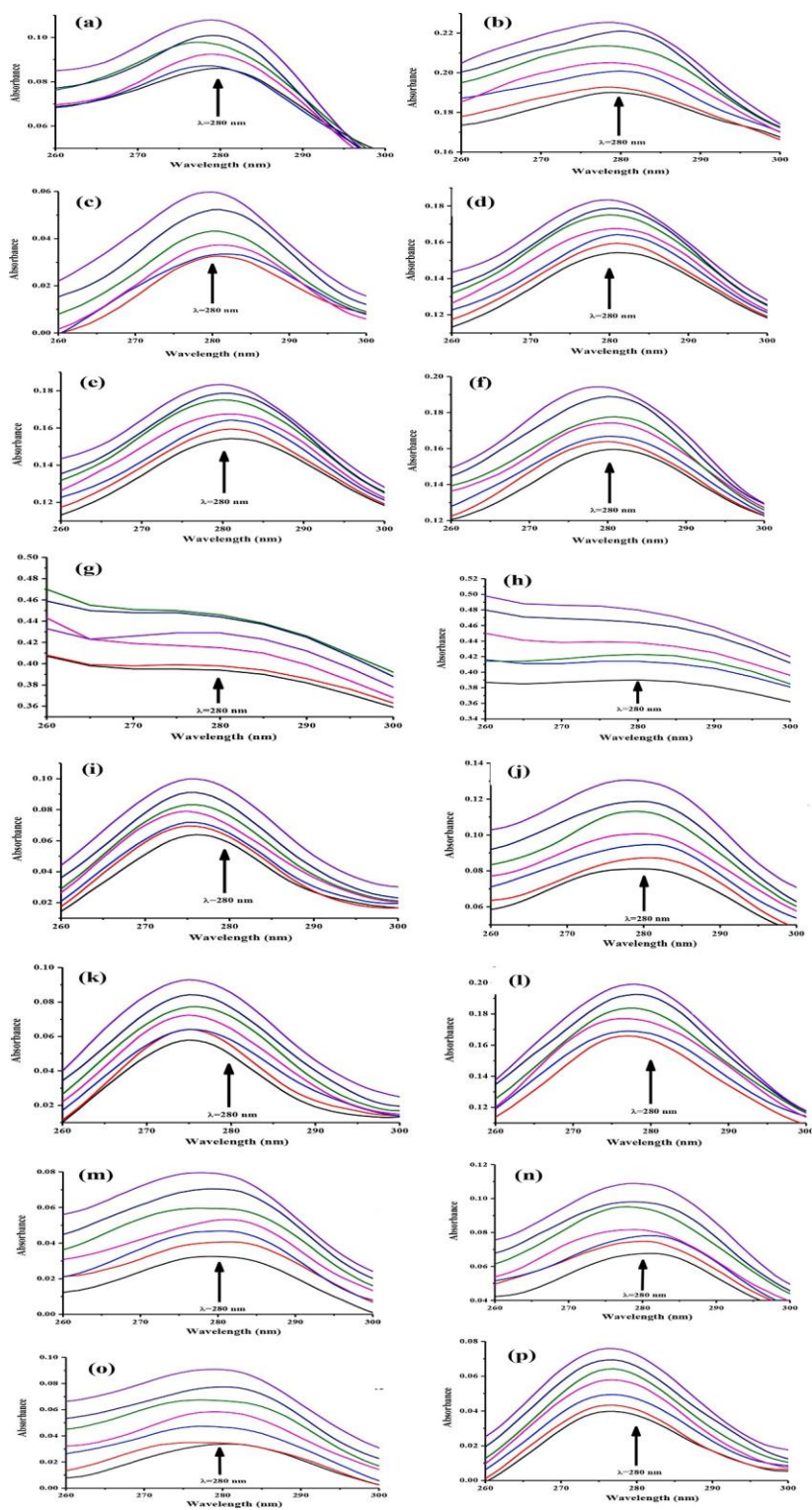
Fig. 8. UV–visible spectra of PSA in serum medium with its increasing concentration from 0.50 pg/mL to 5.50 pg/mL in (a) control set; in presence of (b) 1d-Fe-Gr, (c) dextrose, (d) dextrose with 1d-Fe-Gr, (e) cholesterol, (f) cholesterol with 1d-Fe-Gr, (g) bilirubin, (h) bilirubin with 1d-Fe-Gr, (i) actrapid, (j) actrapid with 1d-Fe-Gr, (k) huminsulin, (l) huminsulin with 1d-Fe-Gr, (m) actrapid **+** dextrose, (n)actrapid **+** dextrose with 1d-Fe-Gr, (o) huminsulin **+** dextrose, (p) huminsulin **+** dextrose with 1d-Fe-Gr.

disorder induced D band in its Raman spectra indicating presence of defects) which in turn acts as decent anchoring sites for the of metal nanocomposites thereby imparting good optical property to them [11,70]. Thus, surface of 1d-Fe-Gr gets charged up in presence of graphene nanoplatelets which in turn can accommodate PSA at its low concentration and rate of change of spectral signal enhances substantially which improves the LOD value.

3.10. Mechanism of sensing of PSA by 1d-Fe-Gr

3.10.1. Fluorescence analysis

In order to investigate the strong interaction of PSA with 1d-Fe-Gr in presence of different biomolecules like glucose, cholesterol, etc., as suggested from UV–vis absorption spectroscopic results, fluorescence spectroscopy was performed to determine the K_{SV} of different simulations. Fig. 11 shows the F_0/F vs. [Q] plot of the interaction between 1d-Fe-Gr and PSA in serum medium both in presence and absence of

Table 3

Limit of detection (LOD) values for PSA in different conditions obtained spectrophotometrically.

Variants	LOD (pg/mL) Conditions*							
	N	D	C	B	A	H	A þ D	H þ D
PSA	1.878	1.669	1.543	4.848	1.242	0.915	1.012	1.008
PSAþ 1d-Fe-Gr	0.878	0.746	0.736	3.499	0.634	0.844	0.984	0.623

Conditions*: N **=** none, D **=** dextrose, C **=** cholesterol, B **=** bilirubin, A **=** actrapid, H **=** huminsulin, (A **+** D) **=** actrapid **+** dextrose, (H **+** D) **=** huminsulin **+** dextrose.
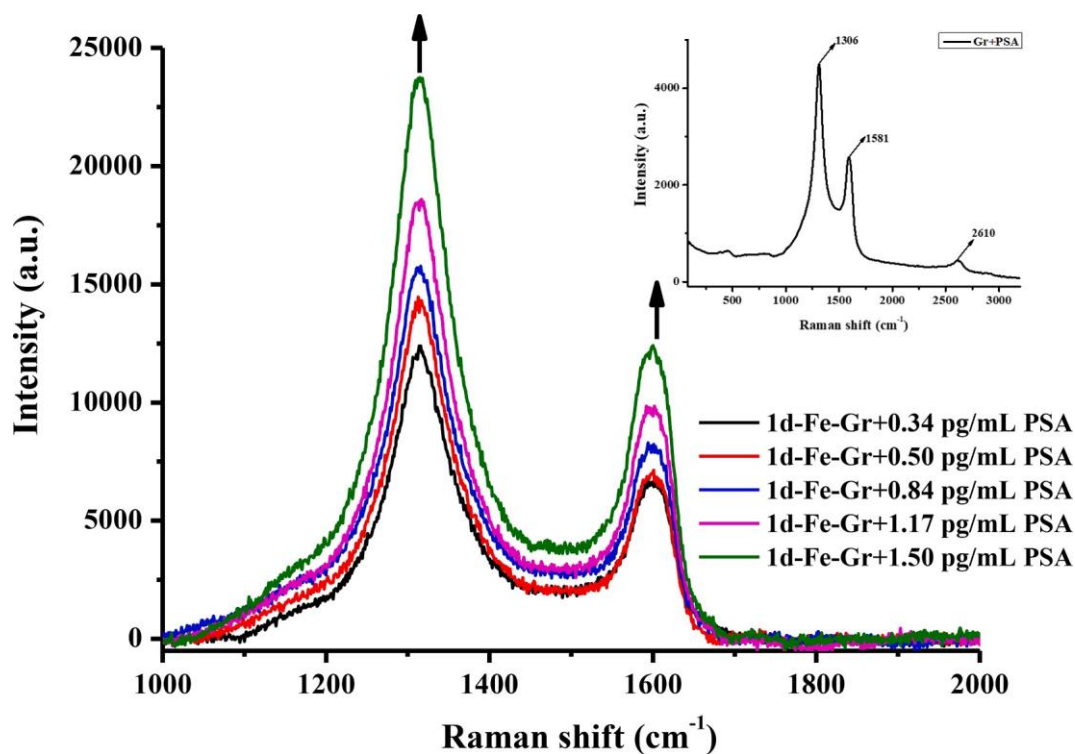

Fig. 9. Concentration dependent Raman spectra of PSA with 1d-Fe-Gr as in reporter, inset shows Raman spectra of graphene nanoplatelet in presence of PSA.
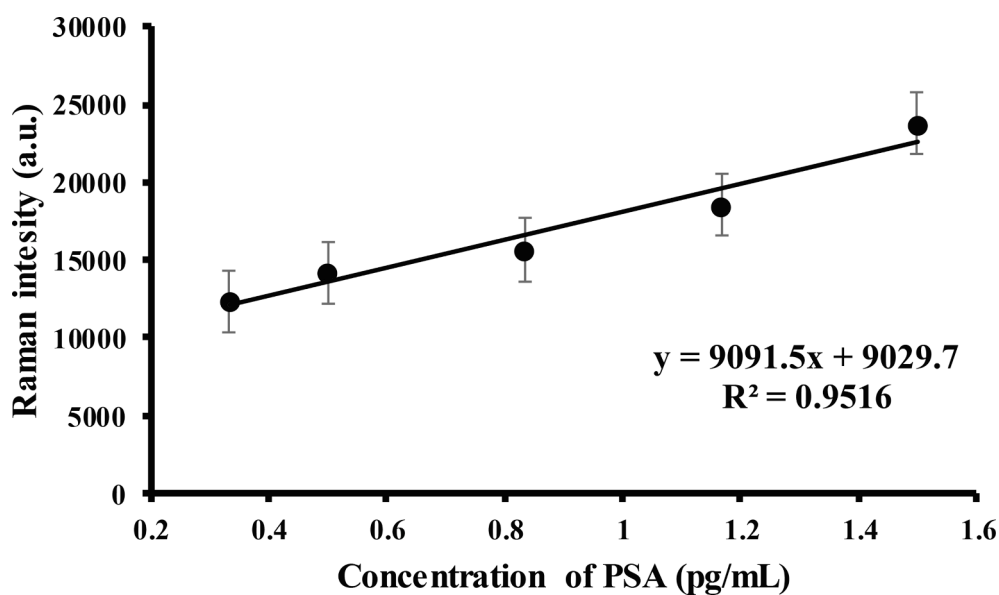

Fig. 10. Linear relationship between Raman spectral intensity and PSA concentration.

Table 4
Limit of detection (LOD) values of CA 19-9.

Variation	LOD (U/mL) Conditions*				
	CA 19-9	CA 19-9 þ D	CA 19-9 þ C	CA 19-9 þ A	CA 19-9 þ H
Without 1d-Fe-Gr	0.082	0.096	0.084	0.079	0.076
With 1d-Fe-Gr	0.172	0.149	0.138	0.131	0.137

Conditions*: D **=** dextrose, C **=** cholesterol, B **=** bilirubin, A **=** actrapid, H **=** huminsulin.

Table 5
Limit of detection (LOD) values of CEA.

Variation	LOD (pg/mL) Conditions*				
	CEA	CEA þ D	CEA þ C	CEA þ A	CEA þ H
Without 1d-Fe-Gr	6.889	14.265	30.146	25.640	17.939
With 1d-Fe-Gr	168.24	36.58	44.170	43.188	38.362

Conditions*: D **=** dextrose, C **=** cholesterol, B **=** bilirubin, A **=** actrapid, H **=** huminsulin.

Table 6
Limit of detection (LOD) values of PSA with other nanocomposite variations.

Variation	Gr	1d þ Gr	1d þ Fe	Gr þ Fe
LOD of PSA (pg/mL)	6.378	4.360	17.619	10.176

glucose, cholesterol to understand their effect on PSA sensing (Fig. S3-S5). It is evident from Table 7 that K_{SV} values of the interaction between 1d-Fe-Gr and PSA both in presence and absence of cholesterol are in comparable range. However, in presence of dextrose in the system, K_{SV} value increases to a great extent which suggests presence of dextrose in the system stabilizes the interaction between 1d-Fe-Gr and PSA. As PSA consists majorly of amino acids (237 amino acid residues), it possesses higher chances of glycosylation in presence of another carbohydrate moiety, dextrose [71]. Thus, dextrose could be covalently attached to

PSA which in turn stabilizes the system. Fluorescence quenching analysis in presence of bilirubin and insulin could not be performed as the biomolecules interfere with the intrinsic fluorescence intensity of PSA.

3.10.2. Conformation study: CD analysis

The far-UV CD spectra of proteins in the range of 190–260 nm help to find any alterations in secondary structure of proteins. CD spectra of PSA, CA 19-9 and CEA in serum medium reveal that these proteins have α-helix rich secondary structure as their corresponding spectra show characteristic double minima at 208 nm and 222 nm and a positive band at 190 nm (both due to nπ* transition of α-helix peptide bond). It could be seen that native structure of PSA remains predominantly α-helical in nature upon its interaction with 1d-Fe-Gr as peak positions in PSA spectra remains unaltered (Fig. 12). A minor change in α-helicity of PSA (from 38.79% to 38.59% in absence and presence of 1d-Fe-Gr respectively) suggests that native conformation of PSA remains nearly unbroken in presence of 1d-Fe-Gr. This proposes that 1d-Fe-Gr binds with amino acid residues of the main polypeptide chain of PSA to a great extent and forms protein-nanocomposite (PSA-1d-Fe-Gr-NC) complex. However, percentage α-helicity content of CA 19-9 and CEA changes significantly in presence of 1d-Fe-Gr which is also reflected from the change in band intensities of their corresponding CD spectra at 222 nm compared to that of PSA (Table 8). This change in α-helicity of CA 19-9 and CEA in presence of 1d-Fe-Gr signifies alteration in secondary structure of these proteins as 1d-Fe-Gr might have perturbed the native conformations of them which in turn causes partial unfolding and loosening of these proteins. Thus, sensing of CA 19-9 and CEA might not be possible due to probable deformation of tryptophan residue of them by 1d-Fe-Gr which is also reflected in the UV–visible spectroscopic data.

Table 7
Different binding constant associated with interaction between PSA and 1d-Fe-Gr at 25 °C.

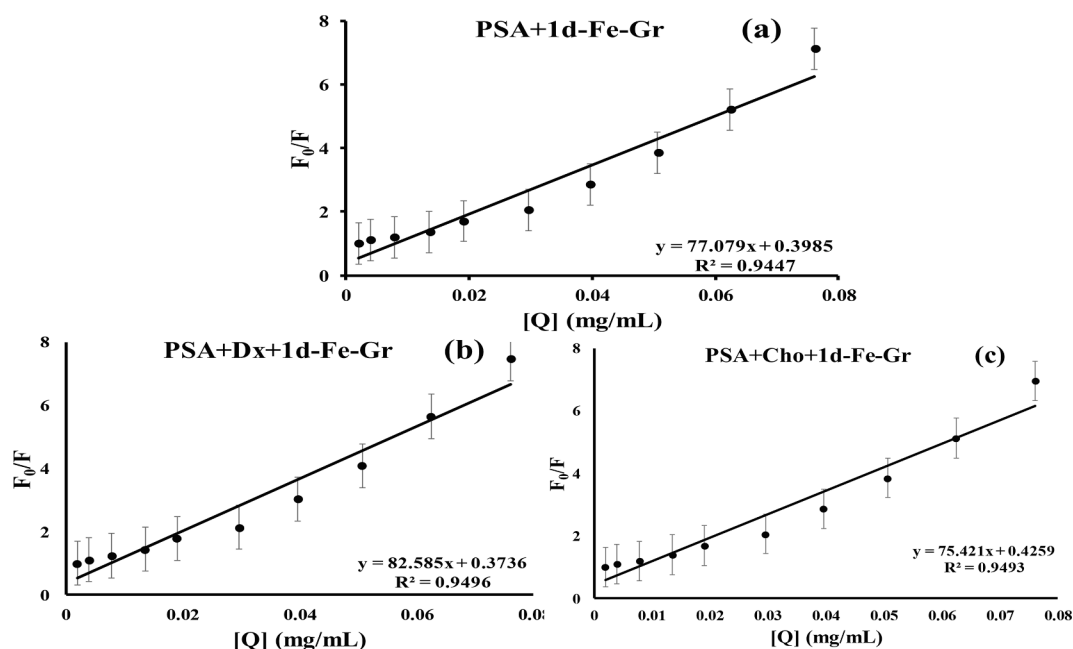| Stern-Volmer constant, K_{SV} (mL/mg)	Conditions		
	None	Dextrose	Cholesterol
PSA **+** 1d-Fe-Gr	77.08	82.58	75.42

Fig. 11. F_0/F vs. [Q] plot of interaction between (a) PSA and 1d-Fe-Gr, (b) in presence of dextrose, (c) in presence of cholesterol.
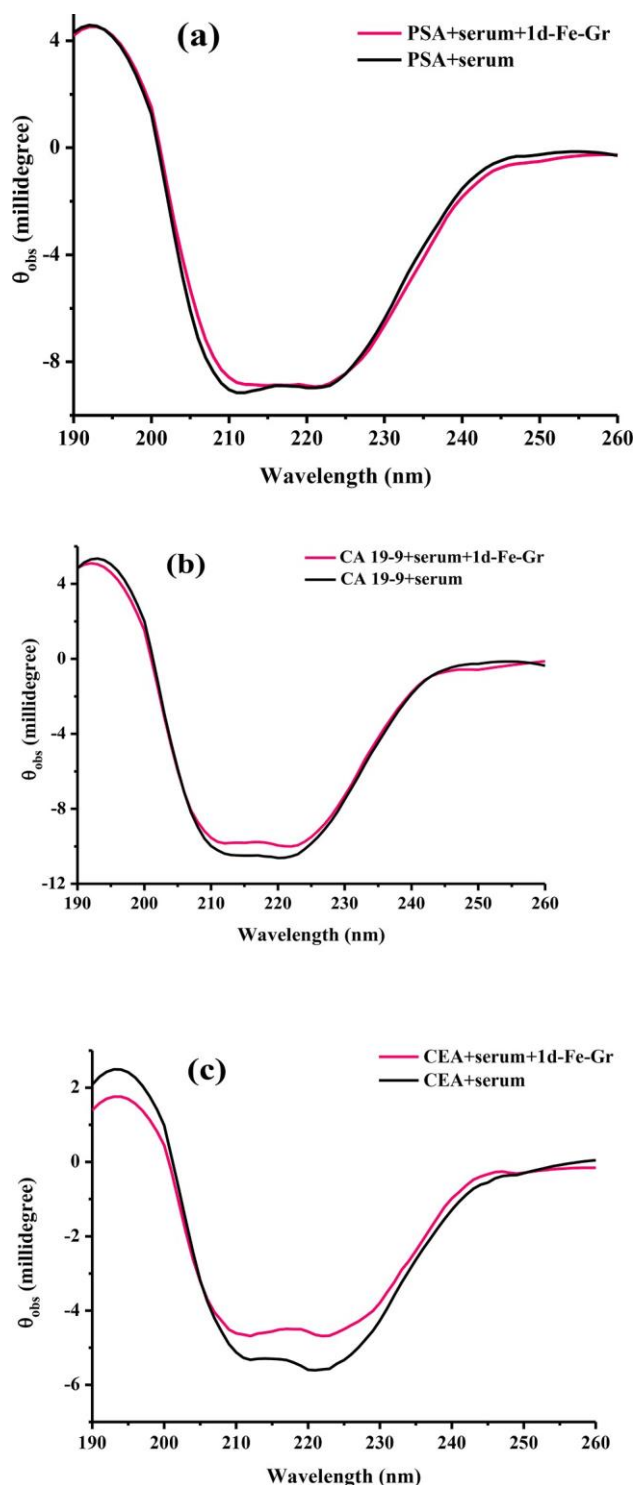
Fig. 12. CD spectra of (a) PSA, (b) CA 19-9 and (c) CEA both in presence and absence of 1d-Fe-Gr in serum medium.

Table 8
α-helicity content of PSA, CA 19-9 and CEA both in presence and absence of 1d-Fe-Gr in serum medium.

	PSA	PSAþ 1d-Fe-Gr	CA 19-9	CA 19-9þ 1d-Fe-Gr	CEA	CEAþ 1d-Fe-Gr
α-helicity (%)	38.78	38.59	57.68	52.38	84.53	69.33

3.11. Theoretical calculations

Molecular docking studies were performed in order to find out the selective interaction of 1d-Fe-Gr towards PSA. Computational studies were carried out using PyMOL for theoretical calculations of the interaction between 1d-Fe-Gr and PSA. Fig. 13 presents the energy minimized complex of 1d-Fe-Gr and PSA which shows clear interactions between them with a high negative binding energy (-980.2 kcal/mol). The interacting amino acid residues of PSA with 1d-Fe-Gr are listed in Table 9. Theoretical calculations show that binding energy of the interaction between 1d-Fe-Gr with CEA and CA 19-9 are -430.7 kcal/mol and -459.0 kcal/mol respectively where tryptophan residue of these biomarkers does not interact with 1d-Fe-Gr (Fig S6-S7, Table S5-S6). The compound 1d is therefore serving multiple purposes in the whole sensing experiment. Firstly, it successfully binds the Fe(III) through its N donor centres to form the complex. Secondly, the complex as a whole, binds with the PSA protein through multiple sites including its tertiary amine group (N,N dimethylaminopropylamine moiety) as well as the Fe(III). The interaction between 1d-Fe-Gr and PSA is thus established through molecular docking and supported by CD spectroscopy.

4. Conclusion

The present work focuses on *in vitro* and selective detection of cancer biomarker PSA using a rapid, simple and economically viable method. Novel use of quinoxaline derivative for cancer biomarker sensing is established here in presence of some pathophysiological conditions like, diabetes, hypercholesterolemia and hepatic disorder. The LOD value of PSA lowers in presence of our synthesized nanocomposite, which lowers more in presence of some biomolecules which are responsible for certain comorbidities. Thus, detection of PSA in the serum samples of the patients suffering from these disorders could also be carried out efficiently. PSA sensing could still be enhanced by the external addition of these biomolecules in the serum samples of cancer patients without these comorbidities. The mechanism of interaction of 1d-Fe-Gr and PSA was studied using Raman, fluorescence and CD spectroscopy. Molecular docking studies support the experimental data, which are involved in interaction with 1d-Fe-Gr. A comparison of the present sensing method has been done with other different methods and tabulated in Table 14.

CRediT authorship contribution statement

Shalmali Basu: Methodology, Investigation, Data curation, Writing – original draft. **Debashree Das:** Methodology, Investigation, Data curation. **Zarina Ansari:** Investigation, Data curation. **Nabakumar Rana:** Investigation. **Bhim Majhi:** Methodology, Data curation. **Dipendu Patra:** Methodology, Data curation. **Ajay Kanungo:** Methodology, Data curation. **David Morgan:** Investigation. **Sanjay Dutta:** Conceptualization, Methodology, Supervision. **Kamalika Sen:** Conceptualization, Methodology, Supervision.

Declaration of Competing Interest

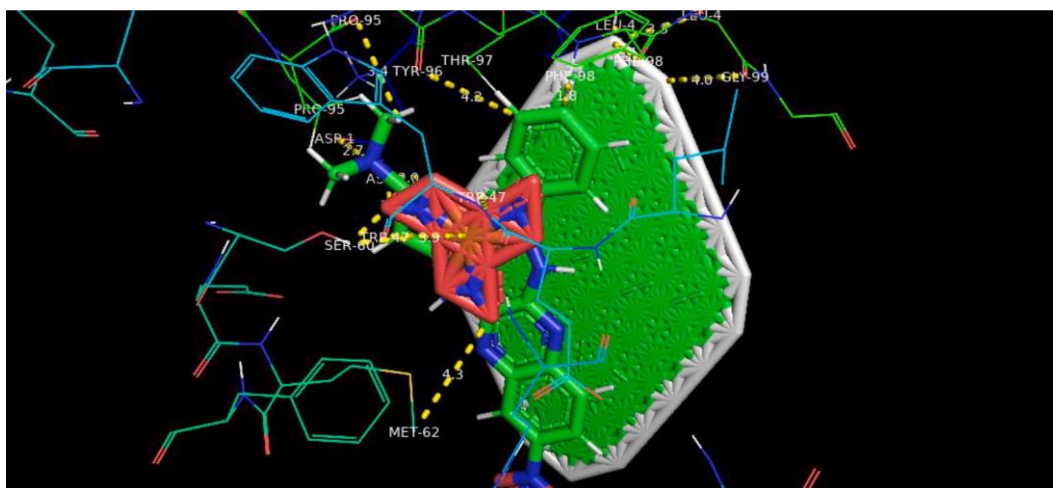**Fig. 13.** Molecular docking of interaction of 1d-Fe-Gr with PSA.

Table 9

List of amino acid residues of PSA interacting with 1d-Fe-Gr.

Binding domain of 1d-Fe-Gr	Amino acid residue	Bond length (Å)
Graphene nanoplatelets	Gly-99	4.0
	Phe-98	2.4
	Leu-4	2.3
		3.3
1d	Asp-1	1.9
		2.7
	Pro-95	3.4
	Tyr-96	4.2
	Phe-98	1.8
Fe(NO₃)₃	Trp-47	2.4
	Met-62	4.3
	Ser-60	1.7
		2.7
	Tyr-96	3.4

Table 14

A comparative study of PSA detection by different methods with proposed method.

Sl No.	Sensor Material	Method	Limit of detection (LOD)	Reference
	AuNP	SERS	~1 pg/mL	[39]
	AuNP-MNP	SERS	5.0 pg/mL	[38]
	Ag@SiO₂@SiO₂-RuBpy	Fluorescence	27 pg/mL	[31]
	EuNP- streptavidin	Time-resolved fluorescence	0.38 ng/L [5]	[36]
	GQDs@Ag	Fluorescence	0.3 pg/mL	[32]
	AuNPs/ rGO/ THI	Electrochemical	10 pg/mL	[72]
	thiolate DNA aptamer /RGO-Au	Electrochemical	3 pg/mL	[73]
	1d-Fe-Gr	Optical	0.879 pg/mL	our work

Appendix A. Supplementary data

Supplementary data to this article can be found online at https://doi.org/10.1016/j.saa.2023.122955.

References

[1] J.A. Pereira, A.M. Pessoa, M.N.D. Cordeiro, R. Fernandes, C. Prudêncio, J.P. Noronha, M. Vieira, Quinoxaline, its derivatives and applications: A State of the Art review, Eur. J. Med. Chem. 97 (2015) 664–672, https://doi.org/10.1016/j.ejmech.2014.06.058.

[2] S. Tariq, K. Somakala, M. Amir, Quinoxaline: An insight into the recent pharmacological advances, Eur. J. Med. Chem. 143 (2018) 542–557, https://doi.org/10.1016/j.ejmech.2017.11.064.

[3] M. González, H. Cerecetto, Quinoxaline derivatives: a patent review (2006–present), Expert Opin. Ther. Pat. 22 (2012) 1289–1302, https://doi.org/10.1517/13543776.2012.724677.

[4] A. Irfan, I. Sabeeh, M. Umer, A.Z. Naqvi, H. Fatima, S. Yousaf, Z. Fatima, A review on the therapeutic potential of quinoxaline derivatives, World, J. Pharm. Res. 6 (2017) 47–68, https://doi.org/10.20959/wjpr201713-9878.

[5] A. Husain, D. Madhesia, Recent advances in pharmacological activities of quinoxaline derivatives, J. Pharm. Res. 4 (2011) 924–929.

[6] A. Irfan, S. Ahmad, S. Hussain, F. Batool, H. Riaz, R. Zafar, K. Kotwica-Mojzych, M. Mojzych, Recent updates on the synthesis of bioactive quinoxaline-containing sulfonamides, Appl. Sci. 11 (2021) 5702, https://doi.org/10.3390/app11125702.

[7] O.O. Ajani, Present status of quinoxaline motifs: Excellent pathfinders in therapeutic medicine, Eur. J. Med. Chem. 85 (2014) 688–715, https://doi.org/

Data availability

Data will be made available on request.

10.1016/j.ejmech.2014.08.034.

[8] M. Montana, F. Mathias, T. Terme, P. Vanelle, Antitumoral activity of quinoxaline derivatives: A systematic review, Eur. J. Med. Chem. 163 (2019) 136–147, https://doi.org/10.1016/j.ejmech.2018.11.059.

[9] S. Bayda, M. Adeel, T. Tuccinardi, M. Cordani, F. Rizzolio, The history of nanoscience and nanotechnology: from chemical–physical applications to nanomedicine, Molecules. 25 (2019) 112, https://doi.org/10.3390/molecules25010112.

[10] S. Basu, K. Sen, A review on graphene-based materials as versatile cancer biomarker sensors, Front, Mater. Sci. 14 (2020) 353–372, https://doi.org/10.1007/s11706-020-0530-8.

[11] J. Zhan, Z. Lei, Y. Zhang Non-covalent interactions of graphene surface: Mechanisms and applications, Chem. 8 (2022) 947-979. DOI: 10.1016/j.chempr.2021.12.015.

[12] S.S.J. Aravind, T.T. Baby, T. Arockiadoss, R.B. Rakhi, S. Ramaprabhu, A cholesterol biosensor based on gold nanoparticles decorated functionalized graphene

nanoplatelets, Thin Solid Films. 519 (2011) 5667–5672, https://doi.org/10.1016/j.tsf.2011.03.032.

[13] V. Kumar, S. Srivastava, S. Umrao, R. Kumar, G. Nath, G. Sumana, P.S. Saxena, A. Srivastava, Nanostructured palladium-reduced graphene oxide platform for high sensitive, label free detection of a cancer biomarker, RSC Adv. 4 (2014) 2267–2273, https://doi.org/10.1039/C3RA41986J.

[14] M.A. Ali, K. Mondal, Y. Jiao, S. Oren, Z. Xu, A. Sharma, L. Dong, Microfluidic immuno-biochip for detection of breast cancer biomarkers using hierarchical composite of porous graphene and titanium dioxide nanofibers, ACS Appl. Mater. Interfaces. 8 (2016) 20570–20582, https://doi.org/10.1021/acsami.6b05648.

[15] M.A. Ali, S. Tabassum, Q. Wang, Y. Wang, R. Kumar, L. Dong, Integrated dual-modality microfluidic sensor for biomarker detection using lithographic plasmonic crystal, Lab Chip. 18 (2018) 803–817, https://doi.org/10.1039/C7LC01211J.

[16] J. Lu, I. Do, L.T. Drzal, R.M. Worden, I. Lee, Nanometal-decorated exfoliated graphite nanoplatelet based glucose biosensor with high sensitivity and fast response, ACS Nano. 2 (2008) 1825–1832, https://doi.org/10.1021/nn800244k.

[17] A. Díaz-Fernández, R. Miranda-Castro, N. de-Los-Santos-Álvarez, E. F. Rodríguez, M. J. Lobo-Castañón, Focusing aptamer selection on the glycan structure of prostate-specific antigen: Toward more specific detection of prostate cancer, Biosens. Bioelectron. 128 (2019) 83-90. DOI: 10.1016/j.bios.2018.12.040.

[18] P. Karami, H. Bagheri, M. Johari-Ahar, H. Khoshsafar, F. Arduini, A. Afkhami, Dual-modality impedimetric immunosensor for early detection of prostate-specific antigen and myoglobin markers based on antibody-molecularly imprinted polymer, Talanta. 202 (2019) 111–122, https://doi.org/10.1016/j.talanta.2019.04.061.

[19] Z. Li, J. Yin, C. Gao, G. Qiu, A. Meng, Q. Li, The construction of electrochemical aptasensor based on coral-like poly-aniline and Au nano-particles for the sensitive detection of prostate specific antigen, Sens. Actuators B Chem. 295 (2019) 93–100, https://doi.org/10.1016/j.snb.2019.05.070.

[20] Z. Yazdani, H. Yadegari, H. Heli, A molecularly imprinted electrochemical nanobiosensor for prostate specific antigen determination, Anal. Biochem. 566 (2019) 116–125, https://doi.org/10.1016/j.ab.2018.11.020.

[21] D.C. Pérez-Ibave, C.H. Burciaga-Flores, M.Á. Elizondo-Riojas, Prostate-specific antigen (PSA) as a possible biomarker in non-prostatic cancer: A review, Cancer Epidemiol. 54 (2018) 48–55, https://doi.org/10.1016/j.canep.2018.03.009.

[22] H. Ehzari, M. Amiri, M. Safari, Enzyme-free sandwich-type electrochemical immunosensor for highly sensitive prostate specific antigen based on conjugation of quantum dots and antibody on surface of modified glassy carbon electrode with core–shell magnetic metal-organic frameworks, Talanta. 210 (2020) 120641, https://doi.org/10.1016/j.talanta.2019.120641.

[23] A.R. Jalalvand, Fabrication of a novel and ultrasensitive label-free electrochemical aptasensor for detection of biomarker prostate specific antigen, Int. J. Biol. Macromol. 126 (2019) 1065–1073, https://doi.org/10.1016/j.ijbiomac.2019.01.012.

[24] L. Dai, Y. Li, W. Wang, X. Luo, D. Wei, R. Feng, T. Yan, X. Ren, B. Du, Q. Wei, A prostate-specific antigen electrochemical immunosensor based on Pd NPs functionalized electroactive Co-MOF signal amplification strategy, Biosens. Bioelectron. 132 (2019) 97–104, https://doi.org/10.1016/j.bios.2019.02.055.

[25] I.G. Subramani, R.M. Ayub, S.C. Gopinath, V. Perumal, M.F.M. Fathil, M. Arshad, Lectin bioreceptor approach in capacitive biosensor for prostate-specific membrane antigen detection in diagnosing prostate cancer, J. Taiwan Inst. Chem. Eng. 120 (2021) 9–16, https://doi.org/10.1016/j.jtice.2021.03.004.

[26] H. Liang, H. Xu, Y. Zhao, J. Zheng, H. Zhao, G. Li, C.P. Li, Ultrasensitive electrochemical sensor for prostate specific antigen detection with a phosphorene platform and magnetic covalent organic framework signal amplifier, Biosens. Bioelectron. 144 (2019), 111691, https://doi.org/10.1016/j.bios.2019.111691.

[27] Y. Chen, P.X. Yuan, A.J. Wang, X. Luo, Y. Xue, L. Zhang, J.J. Feng, A novel electrochemical immunosensor for highly sensitive detection of prostate-specific antigen using 3D open-structured PtCu nanoframes for signal amplification, Biosens. Bioelectron. 126 (2019) 187–192, https://doi.org/10.1016/j.bios.2018.10.057.

[28] Y. Yang, Q. Yan, Q. Liu, Y. Li, H. Liu, P. Wang, L. Chen, D. Zhang, Y. Li, Y. Dong, An ultrasensitive sandwich-type electrochemical immunosensor based on the signal amplification strategy of echinoidea-shaped Au@ Ag-Cu$_2$O nanoparticles for prostate specific antigen detection, Biosens. Bioelectron. 99 (2018) 450–457, https://doi.org/10.1016/j.bios.2017.08.018.

[29] A. Raouafi, A. Sánchez, N. Raouafi, R. Villalonga, Electrochemical aptamer-based bioplatform for ultrasensitive detection of prostate specific antigen, Sens. Actuators B Chem. 297 (2019), 126762, https://doi.org/10.1016/j.snb.2019.126762.

[30] K. Kerman, T. Endo, M. Tsukamoto, M. Chikae, Y. Takamura, E. Tamiya, Quantum dot-based immunosensor for the detection of prostate-specific antigen using fluorescence microscopy, Talanta. 71 (2007) 1494–1499, https://doi.org/10.1016/j.talanta.2006.07.027.

[31] D.D. Xu, Y.L. Deng, C.Y. Li, Y. Lin, H.W. Tang, Metal-enhanced fluorescent dye-doped silica nanoparticles and magnetic separation: A sensitive platform for one-step fluorescence detection of prostate specific antigen, Biosens. Bioelectron 87 (2017) 881–887, https://doi.org/10.1016/j.bios.2016.09.034.

[32] H. Pei, S. Zhu, M. Yang, Kong. R, Y. Zheng, F, Qu Graphene oxide quantum dots@ silver core–shell nanocrystals as turn-on fluorescent nanoprobe for ultrasensitive detection of prostate specific antigen, Biosens. Bioelectron. 74 (2015) 909-914. DOI: 10.1016/j.bios.2015.07.056.

[33] D.C. Albuquerque, V.C. Martins, S. Cardoso, Magnetoresistive Detection of Clinical Biomarker for Monitoring of Colorectal Cancer, IEEE Magn. Lett. 10 (2019) 1–5, https://doi.org/10.1109/LMAG.2019.2951339.

[34] W.Y. Lim, B.T. Goh, S.M. Khor, Microfluidic paper-based analytical devices for potential use in quantitative and direct detection of disease biomarkers in clinical

[35] H. Sohrabi, N. Bolandi, A. Hemmati, S. Eyvazi, S. Ghasemzadeh, B Baradaran., F. Oroojalian, M. R. Majidi, M de la. Guardia , A. Mokhtarzadeh, A. Mokhtarzadeh, A, State-of-the-art cancer biomarker detection by portable (Bio) sensing technology: A critical review. Microchem. J. 107248 (2022). DOI: 10.1016/j.microc.2022.107248.

[36] H. Harma, T. Soukka, T. Lovgren, Europium nanoparticles and time-resolved fluorescence for ultrasensitive detection of prostate-specific antigen, Clin. Chem. 47 (2001) 561–568, https://doi.org/10.1093/clinchem/47.3.561.

[37] L. Tang, S. Li, L. Xu, W. Ma, H. Kuang, L. Wang, C. Xu, Chirality-based Au@ Ag nanorod dimers sensor for ultrasensitive PSA detection, ACS Appl. Mater. Interfaces 7 (2015) 12708–12712, https://doi.org/10.1021/acsami.5b01259.

[38] K. Yang, Y. Hu, N. Dong, G. Zhu, T. Zhu, N. Jiang, A novel SERS-based magnetic aptasensor for prostate specific antigen assay with high sensitivity, Biosens. Bioelectron. 94 (2017) 286-291. DOI; 10.1016/j.bios.2017.02.048.

[39] D. S. Grubisha, R. J. Lipert, H. Y. Park, J. Driskell, M. D. Porter Femtomolar detection of prostate-specific antigen: an immunoassay based on surface-enhanced Raman scattering and immunogold labels, Anal. Chem. 75 (2003) 5936-5943. DOI: 10.1021/ac034356f.

[40] A. Łupicka-Słowik, R. Grzywa, E. Leporowska, D. Procyk, J. Oleksyszyn, M. Sieńczyk, Development and evaluation of an immunoglobulin Y-based ELISA for measuring prostate specific antigen in human serum, Ann. Lab. Med. 39 (2019) 373–380, https://doi.org/10.3343/alm.2019.34.4.373.

[41] Y. Wang, M. Wang, H. Yu, G. Wang, P. Ma, S. Pang, Y. Jiao, A. Liu, Screening of peptide selectively recognizing prostate-specific antigen and its application in detecting total prostate-specific antigen, Sens. Actuators. B Chem. 367 (2022), 132009, https://doi.org/10.1016/j.snb.2022.132009.

[42] S.D. Iancu, R.G. Cozan, A. Stefancu, M. David, T. Moisoiu, C. Moroz-Dubenco, A. Bajcsi, C. Chira, A. Andreica, L.F. Leopold, D. Eniu, A. Staicu, I. Goidescu, C. Socaciu, D.T. Eniu, L. Diosan, N. Leopold, SERS liquid biopsy in breast cancer. What can we learn from SERS on serum and urine? Spectrochim. Acta A Mol. Biomol. Spectrosc. 273 (2022), 120992 https://doi.org/10.1016/j.saa.2022.120992.

[43] S. Chang, S.L. Eichmann, T.Y.S. Huang, W. Yun, W. Wang, Controlled design and fabrication of SERS–SEF multifunctional nanoparticles for nanoprobe applications: morphology-dependent SERS phenomena, J. Phys. Chem. C. 121 (2017) 8070–8076, https://doi.org/10.1021/acs.jpcc.7b00688.

[44] C. Caro, P. Quaresma, E. Pereira, J. Franco, M. Pernia Leal, M.L. García-Martín, J. L. Royo, J.M. Oliva-Montero, P.J. Merkling, A.P. Zaderenko, D. Pozo, R. Franco, Synthesis and characterization of elongated-shaped silver nanoparticles as a biocompatible anisotropic SERS probe for intracellular imaging: theoretical modeling and experimental verification, Nanomater. 9 (2019) 256, https://doi.org/10.3390/nano9020256.

[45] T. Moisoiu, M.P. Dragomir, S.D. Iancu, S. Schallenberg, G. Birolo, G. Ferrero, D. Burghelea, A. Stefancu, R.G. Cozan, E. Licarete, A. Allione, G. Matullo, G. Iacob, Z. Bálint, R.I. Badea, A. Naccarati, D. Horst, B. Pardini, N. Leopold, F. Elec, Combined miRNA and SERS urine liquid biopsy for the point-of-care diagnosis and molecular stratification of bladder cancer, Mol. Med. 28 (2022) 39, https://doi.org/10.1186/s10020-022-00462-z.

[46] C. Caro, F. Gámez, A. P. Zaderenko, Preparation of surface-enhanced raman scattering substrates based on immobilized silver-capped nanoparticles. J. Spectroscop. (2018) 2018. DOI: 10.1155/2018/4127108.

[47] N. Fairley, V. Fernandez, M. Richard-Plouet, C. Guillot-Deudon, J. Walton, E. Smith, D. Flahaut, M. Greiner, M. Biesinger, S. Tougaard, D. Morgan, J. Baltrusaitis, Systematic and collaborative approach to problem solving using X-ray photoelectron spectroscopy, Appl. Surf. Sci. 5 (2021), 100112, https://doi.org/10.1016/j.apsadv.2021.100112.

[48] A. Kanungo, D. Patra, S. Mukherjee, T. Mahata, P.R. Maulik, S. Dutta, Synthesis of a visibly emissive 9-nitro-2, 3-dihydro-1 H-pyrimido [1, 2-a] quinoxalin-5-amine scaffold with large stokes shift and live cell imaging, RSC Adv. 5 (2015) 70958–70967, https://doi.org/10.1039/C5RA12960E.

[49] D.R. Pandeya, A. Mittal, B. Sathian, B. Bhatta, Role of hyperinsulinemia in increased risk of prostate cancer: a case control study from Kathmandu Valley, Asian Pac. J. Cancer Prev. 15 (2014) 1031–1033, https://doi.org/10.7314/apjcp.2014.15.2.1031.

[50] V. Zingales, A. Distefano, M. Raffaele, A. Zanghi, I. Barbagallo, L. Vanella, Metformin: a bridge between diabetes and prostate cancer, Front. Oncol. 7 (2017) 243, https://doi.org/10.3389/fonc.2017.00243.

[51] P. Kachhawa, K. Kachhawa, D. Agrawal, V. Sinha, P.D. Sarkar, S. Kumar, A study of prostate cancer and its association with dyslipidemia, elevated insulin levels in blood, and relative insulin resistance prevalent in South East Asia, J Integr. Nephrol. Androl. 5 (2018) 24, https://doi.org/10.4103/jina.jina_30_17.

[52] D. Das, S. Sen, K. Sen, Caffeine and catechin towards prevention of drug induced oxidation of hemoglobin: a spectroscopic study, Spectrochim. Acta - A: Mol. Biomol. 232 (2020), 118167, https://doi.org/10.1016/j.saa.2020.118167.

[53] H. K. Ardani, C. Imawan, W. Handayani, D. Djuhana, A. Harmoko, V. Fauzia, Enhancement of the stability of silver nanoparticles synthesized using aqueous extract of Diospyros discolor Willd. leaves using polyvinyl alcohol. IOP Conf. Ser.: Mater. Sci. Eng. (2017) 012056). IOP Publishing. DOI: 10.1088/1757-899X/188/1/012056.

[54] N. Kumar, F. Fuloria, Spectroscopy: Fundamentals and Data Interpretation, Studium Press, 2013.

[55] H.R. da Silva, C.M. Quintella, M. Meira, Separation and identification of functional groups of molecules responsible for fluorescence of biodiesel using FTIR

spectroscopy and principal component analysis, J. Braz. Chem. Soc. 28 (2017) 2348–2356, https://doi.org/10.21577/0103-5053.20170088.

[56] T. Togashi, T. Naka, S. Asahina, K. Sato, S. Takami, T. Adschiri, Surfactant-assisted one-pot synthesis of superparamagnetic magnetite nanoparticle clusters with tunable cluster size and magnetic field sensitivity, Dalton Trans. 40 (2011) 1073–1078, https://doi.org/10.1039/C0DT01280G.

[57] M.A. Vargas, J.E. Diosa, E. Mosquera, Data on study of hematite nanoparticles obtained from Iron (III) oxide by the Pechini method, Data Br. 25 (2019), 104183, https://doi.org/10.1016/j.dib.2019.104183.

[58] P.S. Pinto, G.D. Lanza, J.D. Ardisson, R.M. Lago, Controlled dehydration of Fe $(OH)_3$ to Fe_2O_3: developing mesopores with complexing iron species for the adsorption of β-lactam antibiotics, J. Braz. Chem. Soc. 30 (2019) 310–317, https://doi.org/10.21577/0103-5053.20180179.

[59] S. Fekri Aval, A. Akbarzadeh, M.R. Yamchi, F. Zarghami, K. Nejati-Koshki, N. Zarghami, Gene silencing effect of SiRNA-magnetic modified with biodegradable copolymer nanoparticles on hTERT gene expression in lung cancer cell line, Artif. Cells. Nanomed. Biotechnol. 44 (2016) 188–193, https://doi.org/10.3109/21691401.2014.934456.

[60] I. Childres, L. A. Jauregui, W. Park, H. Cao, Y. P. Chen, Raman spectroscopy of graphene and related materials, In New developments in photon and materials research, Jang, J. I., Ed.; Nova Science Publishers, 2013.

[61] S.R. Ahmad, R.J. Young, I.A. Kinloch, Raman spectra and mechanical properties of graphene/polypropylene nanocomposites, Int. J. Chem. Eng. Appl. 6 (2015) 1–5, https://doi.org/10.7763/IJCEA.2015.V6.440.

[62] M. Rashad, F. Pan, Z. Yu, M. Asif, H. Lin, R. Pan, Investigation on microstructural, mechanical and electrochemical properties of aluminum composites reinforced with graphene nanoplatelets, Prog. Nat. Sci.: Mater. Int. 25 (2015) 460–470, https://doi.org/10.3390/nano9081070.

[63] E.C. Sklute, S. Kashyap, M.D. Dyar, J.F. Holden, T. Tague, P. Wang, S.J. Jaret, Spectral and morphological characteristics of synthetic nanophase iron (oxyhydr) oxides, Phys. Chem. Miner. 45 (2018) 1–26, https://doi.org/10.1007/s00269-017-0897-y.

[64] I. Chourpa, L. Douziech-Eyrolles, L. Ngaboni-Okassa, J.F. Fouquenet, S. Cohen-Jonathan, M. Soucé, H. Marchais, P. Dubois, Molecular composition of iron oxide nanoparticles, precursors for magnetic drug targeting, as characterized by confocal Raman microspectroscopy, Analyst. 130 (2005) 1395–1403, https://doi.org/10.1039/B419004A.

[65] X. Zheng, W. Chen, G. Wang, Y. Yu, S. Qin, J. Fang, F. Wang, X.A. Zhang, The Raman redshift of graphene impacted by gold nanoparticles, AIP Adv. 5 (2015), 057133, https://doi.org/10.1063/1.4921316.

[66] F. Venturi, G.A. Rance, J. Thomas, T. Hussain, A low-friction graphene nanoplatelets film from suspension high velocity oxy-fuel thermal spray, AIP Adv. 9 (2019), 025216, https://doi.org/10.1063/1.5089021.

[67] C. Ramirez, M.I. Osendi, Characterization of graphene nanoplatelets-Si3N4 composites by Raman spectroscopy, J. Eur. Ceram. Soc. 33 (2013) 471–477, https://doi.org/10.1016/J.JEURCERAMSOC.2012.09.014.

[68] T. Palaniselvam, H.B. Aiyappa, S. Kurungot, An efficient oxygen reduction electrocatalyst from graphene by simultaneously generating pores and nitrogen doped active sites, J. Mater. Chem. 22 (2012) 23799–23805, https://doi.org/10.1039/C2JM35128E.

[69] NIST X-ray Photoelectron Spectroscopy Database, NIST Standard Reference Database Number 20, National Institute of Standards and Technology, Gaithersburg MD, 20899 (2000), DOI:10.18434/T4T88K, (accessed 2022-09-12).

[70] R. Sujith, P.K. Chauhan, J. Gangadhar, A. Maheshwari, Graphene nanoplatelets as nanofillers in mesoporous silicon oxycarbide polymer derived ceramics, Sci. Rep. 8 (2018) 1–9, https://doi.org/10.1038/s41598-018-36080-1.

[71] J. Malm, H. Lilja, Biochemistry of prostate specific antigen, PSA, Scand. J Clin. Lab. 55 (1995) 15–22, https://doi.org/10.3109/00365519509090559.

[72] B. Wei, K. Mao, N. Liu, M. Zhang, Z. Yang, Graphene nanocomposites modified electrochemical aptamer sensor for rapid and highly sensitive detection of prostate specific antigen, Bios. Bioelec. 121 (2018) 41–46, https://doi.org/10.1016/j.bios.2018.08.067.

[73] G. Mehdipour, J. Shabani Shayeh, M. Omidi, M. Pour Madadi, F. Yazdian, L. Tayebi, An electrochemical aptasensor for detection of prostate-specific antigen using reduced graphene gold nanocomposite and Cu/carbon quantum dots, Biotech. Appl. Biochem 69 (2022) 2102–2111, https://doi.org/10.1002/bab.2271.